Active Vibration Suppression for Wafer Transfer Systems in Semiconductor Fabrication Plants

by

Jiajie Qiu

B.S.E. Mechanical Engineering, University of Michigan (2021)
B.E. Electrical and Computer Engineering, Shanghai Jiao Tong University (2021)

Submitted to the Department of Mechanical Engineering
in partial fulfillment of the requirements for the degree of

Master of Science in Mechanical Engineering

at the

MASSACHUSETTS INSTITUTE OF TECHNOLOGY

June 2023

Author .....
Department of Mechanical Engineering
May 12, 2023

Certified by .....
Kamal Youcef-Toumi
Professor of Mechanical Engineering
Thesis Supervisor

Accepted by .....
Nicolas G. Hadjiconstantinou
Chairman, Department Committee on Graduate Students

Active Vibration Suppression for Wafer Transfer Systems in Semiconductor Fabrication Plants

by

Jiajie Qiu

Submitted to the Department of Mechanical Engineering
on May 12, 2023, in partial fulfillment of the
requirements for the degree of
Master of Science in Mechanical Engineering

Abstract

Vibration suppression is critical in precision mechatronic systems for nanofabrication. In semiconductor plants, automated wafer handling is performed by Overhead Hoist Transport (OHT) vehicles that transport wafers in front opening unified pods (FOUPs). When the wafers are transported in FOUPs, semiconductor chips are at risk of damage by excited small particles due to mechanical vibration, especially if such particles land on the critical area of the wafers. To minimize the vibration excitation force transferred to the FOUP, this thesis focuses on active suppression of the FOUP vibrations to improve the production yield. However, two primary challenges make this problem difficult. First, the OHT vehicle and the FOUP keep traveling, thus the target system is floating with no external anchoring point as a momentum source for control efforts. Second, no sensor attachment is permitted on mass-production FOUPs, which makes feedback control more challenging without measurement. To address the challenges and achieve the goal of reducing FOUP acceleration peaks, an inertia-based counterbalancing system is developed. To validate this system, a customized testbed is built to replicate the acceleration profile of the OHT vehicle in both travel and lateral axes. Additionally, an active vibration suppression system is designed to generate a controllable force on the hand unit. System modeling and identification are conducted using simulation and experiment to identify the system dynamics. Finally, a Disturbance Observer-Based Controller (DOBC) is developed and implemented on the hardware. The experimental results show that the DOBC achieves 38 percent reduction of OHT hand unit vibration and 42 percent reduction of FOUP vibration in the OHT travel direction. Furthermore, the proposed method successfully reduces the multi-axis FOUP-level acceleration peaks, further confirming the effectiveness of the proposed method.

Thesis Supervisor: Kamal Youcef-Toumi
Title: Professor of Mechanical Engineering

Acknowledgments

I would like to thank all those who have contributed to my degree and helped to make this work possible.

First and foremost, I want to express my sincere appreciation to my advisor, Professor Kamal Youcef-Toumi, for his caring nature and mentorship. I get a lot of support and guidance from Kamal and it's my honor to work under his supervision.

I also want to thank my labmates in the Mechatronics Research Lab for their collaboration and friendship, which have made my experience in our lab enjoyable and rewarding. A special thanks to our postdoctoral researcher, Fangzhou, for all the guidance and help. I am really impressed by his knowledge and expertise.

I would like to acknowledge the support from my sponsor, Samsung Electronics Co., Ltd. (IO211005-08995-01). In particular, I am grateful to Dr. Hongjing Kim, the research scientist from Samsung, for his help and efforts.

Finally, I am thankful to my parents, Cuiwen Qian and Yuchen Qiu. Their support has enabled me to focus entirely on my research and studies. I also would like to thank my friend, Rika, for her accompany and emotional support, and I am grateful for her kindness. Last but not least, I want to thank my cat, Mimi, the fluffy queen, for her being my cat.

Contents

List of Figures

List of Tables

Chapter 1

Introduction

The Overhead Hoist Transport (OHT) system is widely utilized in modern semiconductor fabrication plants for the transportation of 300 mm wafers between numerous processing steps. The OHT vehicles move along tracks mounted on the ceiling of the semiconductor fabrication plant and can carry wafers in Front-Opening Unified Pods (FOUPs). The FOUP is a standard wafer carrier for 300 mm wafers, with a capacity to hold up to 25 wafers per carrier. OHT vehicles carry FOUPs using OHT hand units [3, 4]. Figure 1-1 illustrates the schematic diagram of the OHT vehicle, OHT hand unit, and FOUP interface.

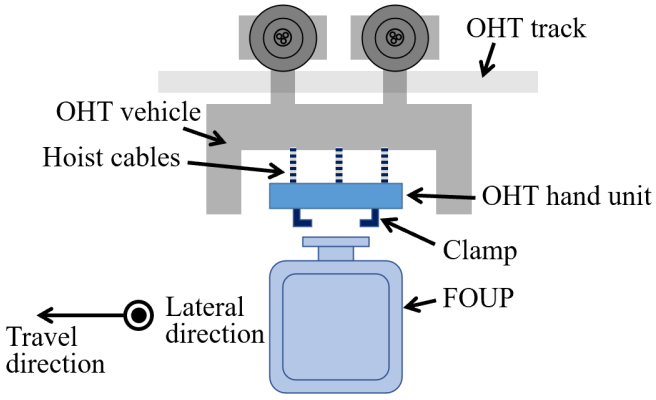

Figure 1-1: Schematic representation of the interface between the OHT vehicle, hand unit, and FOUP. [1]

Due to the significant number of transportation requirements, it is important to

maintain the wafers intact during transit. Samsung Electronics Co., Ltd. operates over 8,000 OHT vehicles in more than 28 fabrication plants worldwide, covering a total travel distance of 644,000 km per day. Given that semiconductor manufacturing involves several hundred processing steps, every wafer must be transported through the OHT system multiple times between every process step. Thus, it is crucial to preserve the wafers intact during transport.

Maintaining a low vibration level on the FOUP during transport is essential. Researchers at Samsung Electronics identified that the transferred vibration from OHT vehicles to FOUPs is a significant factor affecting wafer quality management. Dust particles inside the FOUP and from the bottom of the wafers can be excited by the vibration, which will cause damage to semiconductor products if they land on critical areas of the wafers [5, 6, 7]. With the continued advancement of semiconductor miniaturization technology, the current vibration reduction strategy of Samsung Electronics using passive damping materials has reached a saturation point, and its performance is inadequate. Therefore, this thesis proposes the development of an active vibration control technique to achieve further reductions in vibration levels.

1.1 Literature review of vibration suppression

Vibration suppression is a broad research field with numerous applications such as construction, transportation, and precision engineering. In the field of building structures vibration control, various types of Tuned Mass Damper (TMD) systems have been utilized as an innovative way [8, 9, 10]. Additionally, active vibration isolation strategies that combine sky-hook spring and sky-hook damper have been studied and applied to various systems, such as car suspension, scanning probe microscopy, and optical tables [11, 12, 13].

For actively suppressing vibration in the FOUP, Tsai et al. suggested an experimental OHT system. This system used a triplet of double-link arms to transport the FOUP, rather than the conventional hoist cables utilized in typical OHT vehicles [14]. By applying a composite controller to this new design, it was possible to

reduce shock, tilt, and high-frequency excitation transferred to the FOUP during transport. However, this experimental design cannot be implemented in actual semiconductor fabrication plants in the real world due to the presence of hoist cables in these facilities.

To enhance the performance of controllers for vibration suppression, Tokoro et al. proposed a state feedback control approach based on actual observable states using suspension stroke sensors of a gasoline engine vehicle [15]. Through experiments, the proposed controller successfully suppressed the pitching and bouncing motion of the vehicle body. Furthermore, Yu et al. employed a disturbance observer-based control method to control a four-wheel steering vehicle [16]. This disturbance observer-based control proved helpful in ignoring nonlinear dynamics and handling exogenous disturbances.

1.2 Unique challenges in the OHT vibration suppression task

The OHT-hand unit-FOUP system presents two unique challenges compared to classical vibration suppression tasks:

1. Firstly, there are no external anchoring points that can be utilized as a momentum source during transportation when The OHT vehicles and the FOUPs keep traveling and the target system is floating. This is different from large-scale static building or optical table applications. Additionally, suppression of the FOUP in-plane vibration levels along traveling and lateral directions has more stringent requirements compared to vehicle applications.

2. Secondly, the acceleration level of the FOUP cannot be directly measured, which sets this control problem apart from other situations where direct state observation is possible. This is due to the current design restrictions in semiconductor fabrication plants, where sensor attachments are not allowed on mass-production FOUPs.

1.3 Main contribution of the thesis

To suppress the vibration on the FOUP during transportation, the main contributions of this work are listed below. The single-axis work is published as a journal paper [2], and the multi-axis work is accepted by the 2023 IEEE/ASME International Conference on Advanced Intelligent Mechatronics [1].

1. Development and characterization of a vibration generation testbed for the OHT hand unit-FOUP system. The testbed is capable of generating vibrations in both the travel and lateral directions simultaneously, to replicate the motions measured from the OHT hand unit during factory operations.

2. Design and implementation of an onboard active vibration suppression system. It is capable of applying controllable inertia force to the OHT hand unit in both travel and lateral directions simultaneously. The inertia force addresses the challenge of suppressing vibration in both the travel and lateral directions simultaneously without external anchoring points.

3. Development of a reproducible system identification procedure for the disturbance observer design. This enables the proposed active vibration suppression technology to be applicable in factories without significant modifications.

4. Design of a disturbance observer-based controller (DOBC) for travel direction vibration control. Both hand unit displacement and FOUP acceleration are suppressed, which is validated with experiments. It allows FOUP-level vibration suppression without direct measurement of the FOUP acceleration.

5. Extension of the active vibration suppression controller to the multi-axis version and the experimental validation of the controller on both OHT displacement and FOUP acceleration. It can suppress the hand unit and FOUP vibration in both travel and lateral directions simultaneously, which demonstrates the effectiveness of the approach for practical application in semiconductor fabrication plants.

It is important to note that this work first focuses on controlling the vibration displacement of the hand unit in the traveling direction (referred to as X-axis) when the disturbance was applied only to the same axis [2]. The work is later extended to a multi-axis version [1], as the disturbance in the lateral axis (referred to as Y-axis) will also affect the X-axis motion and vice versa. This is due to the fact that the hand unit is suspended in the OHT vehicle through three hoist cables, as shown in Figure 1-1. Therefore, the original system and testbed design (to be introduced in chapter 2) can result in motion coupling between the X and Y axis. As a result, the controller should not only compensate for the disturbance affecting the designed axis but also resist all dynamic effects from the orthogonal axis. The twisting mode may also be excited due to a small misalignment in the external force source on the testbed, but this is not significant in practical applications and thus is not considered.

1.4 Organization of the thesis

The thesis is structured as follows:

Chapter 2 presents the design and specification of the vibration generation testbed (which is designed to replicate the real OHT track system), and the implementation of the controller hardware. The output force bandwidth of the vibration actuation is also verified in this chapter.

Chapter 3 develops a linear dynamic system model and applies system identification techniques to identify the systems. In this work, due to the complexity of the multi-axis testbed-hand unit-FOUP system, a systematic approach is employed to gradually increase the complexity of the system. The testbed-hand unit system without the FOUP is first analyzed. After that, the FOUP is clamped under the hand unit, and the new system is identified. Both the single-axis system (where only the X-axis vibration generation actuator is connected to the hand unit) and the multi-axis system (where both actuators are connected to the OHT hand unit with stingers) are identified in this chapter. It's important to note that the engagement of the orthogonal axis vibration generation actuator acts as an extra connection be-

tween the testbed and the hand unit, and thus the dynamic of the multi-axis system is different from the single-axis system. Numerical transfer functions are fitted for controller design, and a disturbance input force profile is generated in this chapter.

Chapter 4 designs and implements controllers for active vibration suppression tasks. In this chapter, the progress towards the development of vibration control techniques for the hand unit-FOUP system is presented in a step-by-step approach. First, the PID controller and disturbance observer-based controller (DOBC) are chosen as suitable types of control techniques. Next, a PID controller and a DOBC are designed and implemented for the testbed-hand unit system, and their performance are compared. Subsequently, the FOUP is clamped under the hand unit, and the controller design is extended to the testbed-hand unit-FOUP system. The DOBC for the X-axis (travel direction) is first designed and implemented to validate that the FOUP acceleration will be suppressed by the designed vibration suppression technique. The multi-axis DOBC is then designed for the testbed-hand unit-FOUP system in both axes and implemented to show that it can suppress the hand unit and FOUP vibration in both travel and lateral directions simultaneously.

In the last chapter of the thesis, Chapter 5, the overall findings of the research are summarized, and the future directions to enhance the vibration control performance are suggested.

Chapter 2

Hardware System Design

The focus of the hardware system design in this study is on the vibration generation testbed and the active vibration suppression system, which are designed around the OHT hand unit carrying a FOUP. The hoist cables on the hand unit are necessary to load or unload FOUPs at target locations that are approximately 8 m apart in height. A pair of clamps is located beneath the vertically suspended OHT hand unit to clamp the FOUP. The main source of vibration transferred to the FOUP is attributed to the travel motion of OHT vehicles. The Samsung Automated Material Handling System (AMHS) team previously conducted vibration transfer path analysis (TPA) studies, which indicated that the OHT hand unit was the dominant path for the vibration transmitted to the FOUP [17, 18]. As a result, the hand unit is chosen as the design domain for active vibration control.

Section 2.1 presents the hardware design of the multi-axis vibration generation testbed that can replicate the vibration of the OHT system. Section 2.2 describes the hardware design of the onboard multi-axis vibration suppression actuators that are used to apply controllable inertia force on the hand unit. Section 2.3 shows the implementation of the data acquisition system. Furthermore, the output force bandwidth is verified in section 2.4, with the actuator output force bandwidth found to exceed 500 Hz. This value is much higher than the mechanical system bandwidth, which demonstrates that the designed vibration generation testbed is suitable for conducting the necessary research.

2.1 Vibration generation testbed mechanical design

The vibration generation testbed is designed and constructed to mimic the vibration of the OHT system. Specifically, the acceleration signal measured from an OHT hand unit during the OHT vehicle travel on the track in the factory is replicated on the hand unit hoisted on the testbed. However, it is impractical to replicate the entire OHT track system in the laboratory environment. Hence, only the hand unit assembly is utilized as the design domain, and a suitable actuator is employed to generate the input vibration. This system provides precise control of the vibration input force to simulate various track and driving conditions of the OHT system. Figure 2-1 displays the computer-aided design (CAD) and the actual testbed.

In order to generate the desired vibration signal with a target bandwidth of 500 Hz, appropriate actuators must be carefully selected. For this purpose, two voice coil actuators (VCAs) with matching force and bandwidth characteristics are chosen to act as the vibration generation actuators for the travel direction (X-axis) and lateral direction (Y-axis). Specifically, the selected VCAs are identical (VCAR0436-0250-00A; SUPT Motion), and their detailed specifications are listed in Table 2.1. Additionally, the VCAs are spring-loaded to establish a neutral position for the system.

	stroke [mm]	force constant [N/A]	force (P) [N]	force (C) [N]
Actuation	25.4	30	220	68.2
Control	22.4	6.8	33	13.5

Table 2.1: VCA specification. "Actuation" refers to the vibration actuation VCA mentioned in Figure 2-1, while "Control" refers to the vibration control VCA mentioned in Figure 2-2. "force (P)" refers to the maximum peak force, while "force (C)" refers to the maximum continuous force.

To maintain the alignment of VCAs, the vibration generation VCAs are connected to the hand unit using modal stingers (2155G12; The Modal Shop, Inc.). The stingers are designed to be rigid in the axial direction and flexible in the radial direction, which prevents any perpendicular disturbances from affecting the alignment of the VCA coils and magnets, while allowing the actuator force to be transmitted in the axial direction. Additionally, linear encoders (IT3402L; Prologue Technology) are

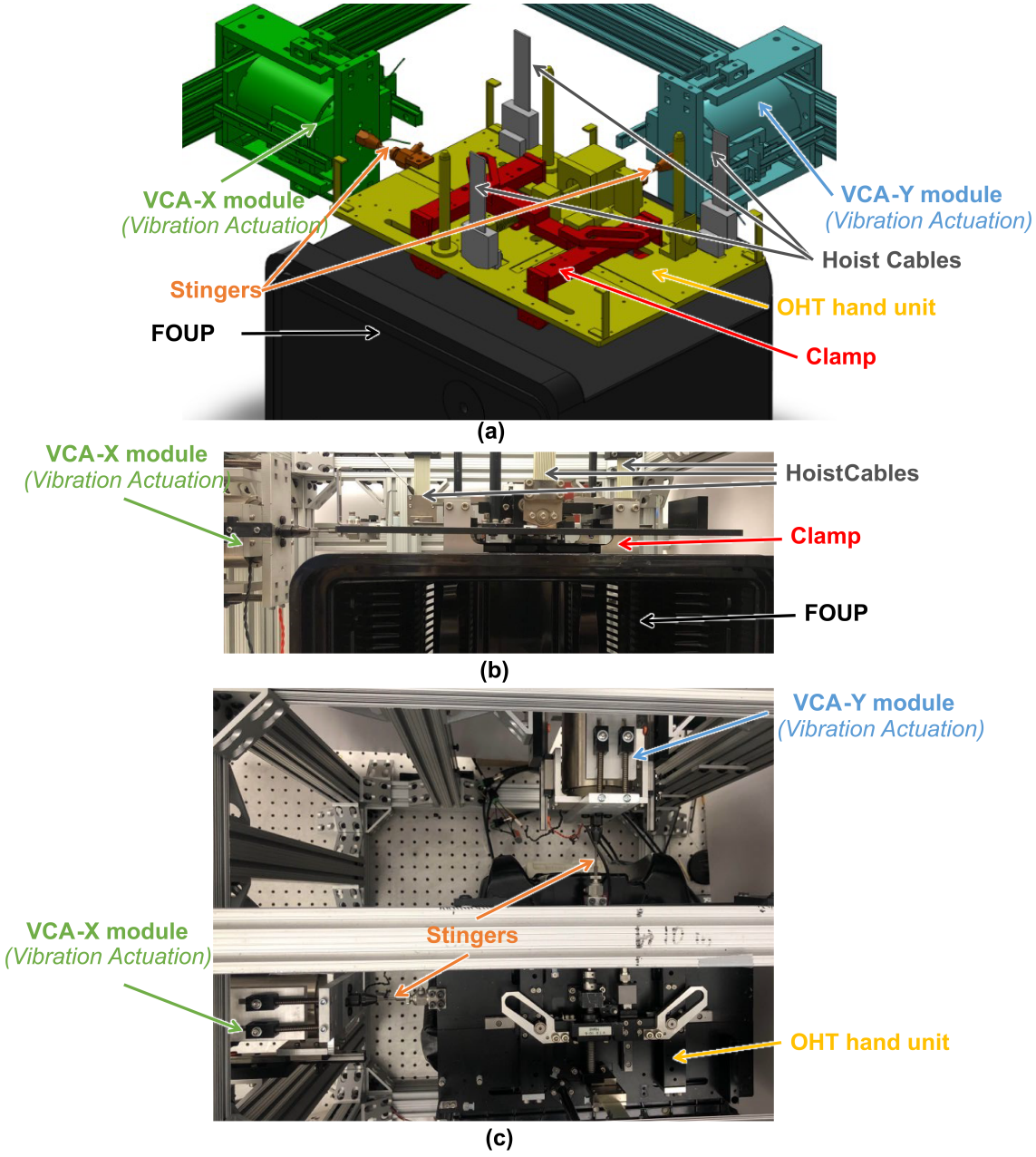

Figure 2-1: (**a**) CAD representation of the vibration generation testbed, and (**b**) a front view of the assembled testbed. (**c**) a top view of the assembled testbed. [1]

installed on the VCAs to provide precise position measurement, with a programmed resolution of 1.25 μm per count, which gives sufficient resolution and a high allowed travel speed of up to 4 m/s. To further record the controller performance of the system, two triaxial accelerometers (3713F1110G; PCB Piezotronics) are placed on the hand unit and inside the FOUP to measure the acceleration. Table 2.2 shows all the sensors, actuators, and data acquisition (DAQ) instruments used in this research.

Type	Component	Manufacturer	Part Number
Sensors	linear encoder	Prologue Technology	IT3402L
	triaxial accelerometer	The Modal Shop, Inc.	3713F1110G
	IEPE force sensor	The Modal Shop, Inc.	208c02
Actuators	actuation VCA	SUPT Motion	VCAR0436-0250-00A
	control VCA	SUPT Motion	VCAR0033-0224-00A
	extension spring	McMaster-Carr	5108N31
	modal stinger	The Modal Shop, Inc.	2155G12
	chuck assembly	The Modal Shop, Inc.	2100E14
DAQ	actuation CompactRIO	National Instrument	cRIO-9074
	control CompactRIO	National Instrument	cRIO-9038
	H-bridge motor driver	National Instrument	NI9505
	digital IO module	National Instrument	NI9402
	analog input module	National Instrument	NI9205
	analog output module	National Instrument	NI9263

Table 2.2: List of components

2.2 Vibration suppression system mechanical design

To suppress vibrations, two smaller VCAs (VCAR0033-0224-00A; SURP Motion) are chosen for inertia force-based counterbalancing application for both the X and Y axes. Figure 2-2 displays the CAD and the actual system. By pushing and pulling the VCA magnets (moving mass), the designed vibration suppression system can apply controllable reaction force to the hand unit to deliver the control effort. The specification is also listed in Table 2.1. These VCAs are monitored by two linear encoders (IT3402L; Prologue Technology) for position tracking. The design of the vibration suppression system takes into account the limited space available in an

existing OHT system and can be implemented in the actual system without significant modifications.

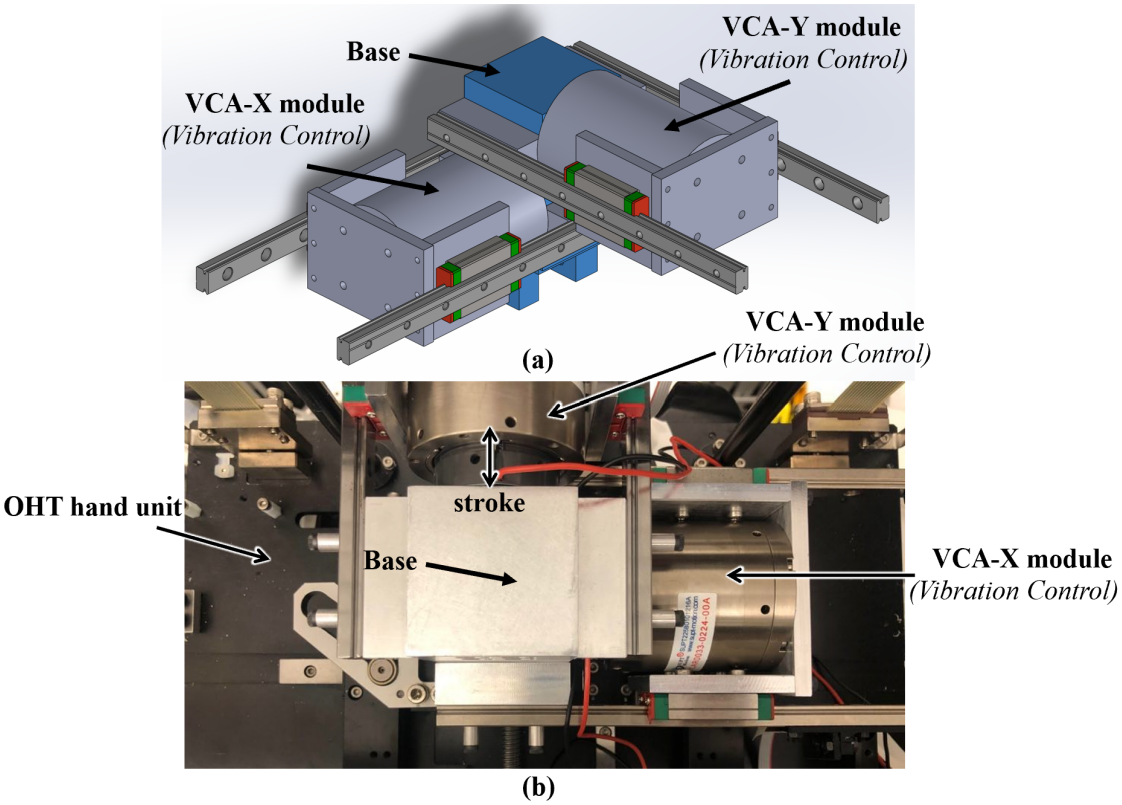

Figure 2-2: (**a**) CAD representation of the vibration suppression actuator, and (**b**) a top view of the assembled vibration suppression system installed on the hand unit. [1]

The maximum amount of momentum that can be generated by the inertia-based vibration suppression system is restricted by the relatively small mass of the moving parts and the limited distance they can travel. To prevent any additional disturbances to the system, it is important to avoid collisions between the moving mass (the VCA magnet mounted on linear bearings) and the base.

2.3 Instrumentation design

Suitable data acquisition and actuator drivers with high enough bandwidth must be chosen to connect and communicate with both the vibration generation testbed and the vibration suppression system. The National Instrument (NI) compact RIO

system is a powerful platform for data acquisition and control applications, and thus is chosen for this purpose (See Figure 2-3). The cRIO-9074 chassis is used to control the vibration generation testbed, while the vibration suppression system is controlled by a cRIO-9038 equipped with a more powerful field programmable gate array (FPGA) to enable high-speed processing and the implementation of more complex control algorithms.

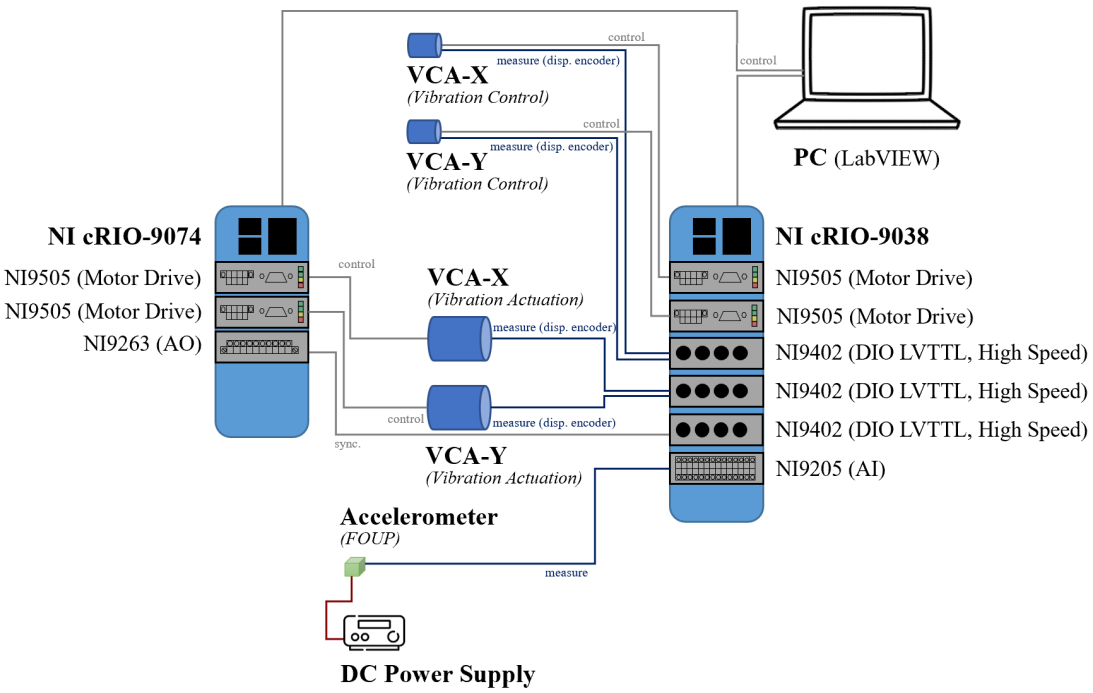

Figure 2-3: Schematic diagram of the mechatronic connection for the vibration generation testbed and the vibration suppression actuators. [1]

As listed in Figure 2-3, various IO modules are utilized. The H-bridge motor drivers (NI9505) enable precise control of the VCAs, while the digital IOs (NI9402) and analog input module (NI9205) allow for precise measurement and monitoring of system parameters, such as the displacement of the VCA and the hand unit, and the acceleration of the hand unit and the FOUP. The analog output module (NI9263) is used to send synchronization signals between the two compact RIO chassis. All the DAQ instruments are listed in Table 2.2.

2.4 Output force bandwidth verification

To ensure that the force output from the vibration actuation VCA meets the required 500 Hz bandwidth, an initial testbed is designed for output force bandwidth verification. The testbed is illustrated in Figure 2-4, which consists of a VCA unit connected to a stinger, with the other end of the stinger connected to a force sensor attached to a wall. The back bar connecting the VCA to the ground in this testbed is the same as the one seen in Figure 2-1 and can be seen as a cantilever.

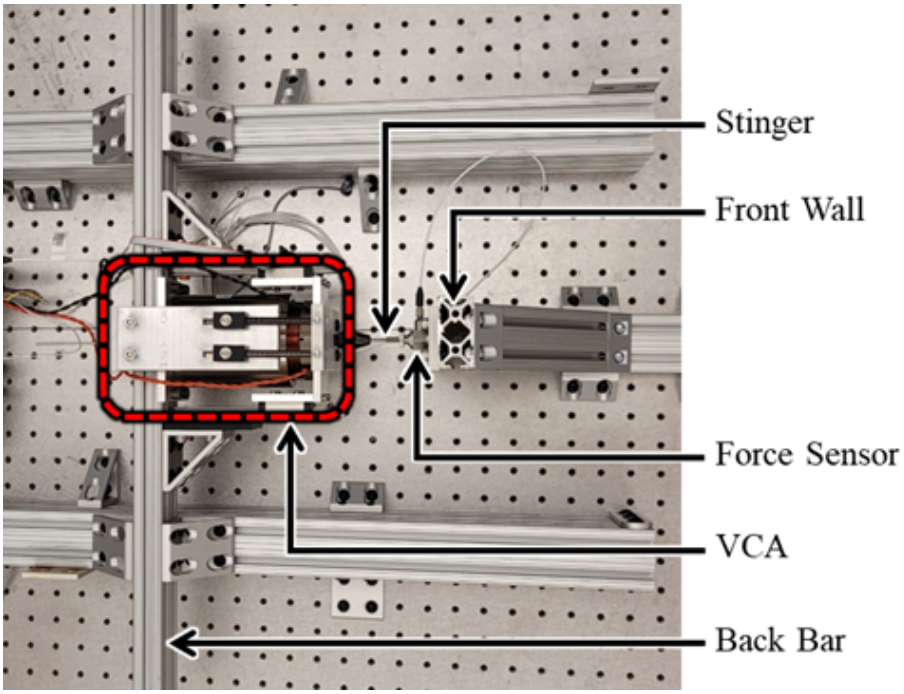

Figure 2-4: The verification testbed used to verify the bandwidth of the output force. [2]

A frequency sweep from 10 Hz to 1000 Hz at intervals of 1 Hz interval is conducted with the lock-in filter (the detail of which will be introduced in section 3.2.1) to verify the output force bandwidth. The bode plot, which relates the VCA input current to the stinger output force, is presented in Figure 2-5. The resonant peaks and anti-resonant peaks in the plot suggest that the system is comprised of multiple mass-spring-damper systems connected together, potentially with dynamics from the aluminum frame structures and the spring-loaded VCA mechanical dynamics.

The observed anti-resonant peak initially had a frequency lower than 500 Hz,

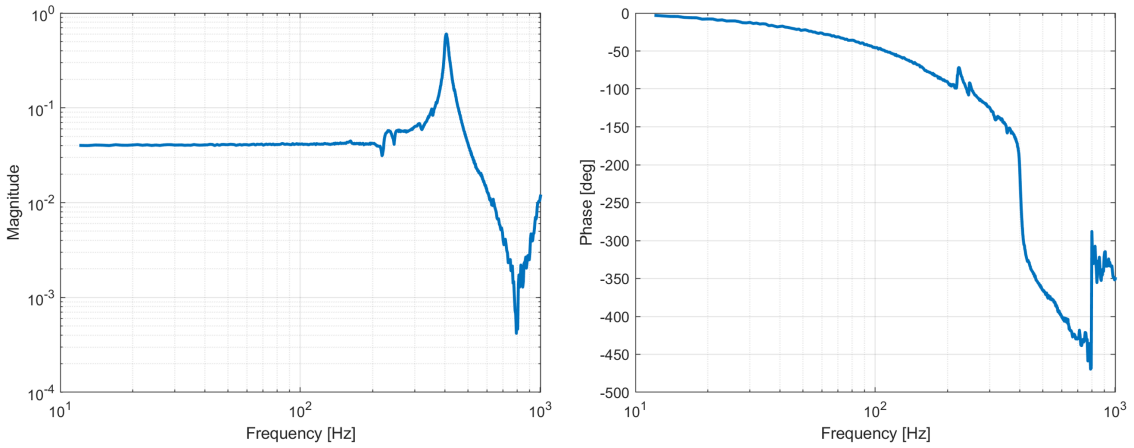

Figure 2-5: Bode plot showing the relationship between the input current and output force of the updated testbed. [2]

which limited the output force bandwidth. We put forward the hypothesis that the back bar and the front wall are not rigid enough. To address this, the support structures are reconfigured by decreasing the distance between the two support bars and reinforcing the front wall. This resulted in a successful shift of the frequency of the anti-resonance peak beyond 500 Hz, as shown in Figure 2-5, thereby meeting the design requirement.

500 Hz is much higher than the mechanical system bandwidth, enabling the dynamic model of the actuators to be simplified as a gain for the relevant frequency range. Similarly, the encoder and accelerometer models could also be simplified as constant gains, resulting in a total bandwidth of 500 Hz as required.

2.5 Summary

This chapter focuses on the hardware system design of the vibration generation testbed and the active vibration suppression system, which are designed around the OHT hand unit carrying a FOUP. The hand unit is the main source of vibration transferred to the FOUP, and thus is chosen as the design domain for active vibration control. The testbed is designed to generate vibrations to the hand unit in multiple axes simultaneously to replicate the hand unit motion in factory operations. Stingers

are utilized to transmit the input force while maintaining the VCA alignment. The vibration suppression system utilizes the inertia force as the control effort to solve the challenge that there exist no external anchoring points as momentum sources. The testbed is verified to have an actuator output force bandwidth exceeding 500 Hz, demonstrating its suitability for conducting the necessary research.

Chapter 3

System Characterization

In this chapter, the focus is on modeling and identifying the dynamics of the system, which is crucial for understanding the system behavior and designing a suitable controller. Firstly, in section 3.1, the dominant dynamic of the system is linearized into a lumped parameter model, and a corresponding parametric transfer function is derived. Next, in section 3.2, the magnitude and phase of the system at different frequencies are obtained through a sinusoidal input frequency sweep. Numerical transfer functions are fitted to the measurement data based on the parametric equations. Finally, in section 3.3, an algorithm to produce the current reference profile for the VCA to generate the desired vibration acceleration profile is presented.

In this study, due to the complexity of the multi-axis testbed-hand unit-FOUP system, a systematic approach is employed to gradually increase the complexity of the system. The approach begins with a simplified version of the system, which is the testbed-hand unit system in the travel direction (X-axis), and then additional components are added incrementally, such as the FOUP and the Y-axis vibration actuator. This approach enables a step-by-step understanding of the system dynamics and facilitates more accurate modeling and identification. Specifically, the identification process starts by verifying the model for the testbed-hand unit system. Then, the FOUP is added to the system, and the single-axis testbed-hand unit-FOUP system dynamics is determined, with the other axis vibration actuator disconnected from the hand unit. Finally, the identification of the multi-axis system is carried out when

both axes are connected to the hand unit with stingers.

Equation (3.1) reveals the presence of four transfer functions, H_{xx}, H_{xy}, H_{yx}, and H_{yy}, which link the two input forces F_x and F_y (generated by VCAs to mimic real-world disturbances) and the output hand unit displacements X and Y. The primary linear dynamics that require control are H_{xx} and H_{yy} when the axes are orthogonal. However, the coupled H_{xy} and H_{yx} exist and are highly nonlinear owing to the twisting motion due to certain constraints in the testbed design. Therefore, they are treated as additional disturbance sources during control.

$$\begin{bmatrix} X(s) \\ Y(s) \end{bmatrix} = \begin{bmatrix} H_{xx}(s) & H_{xy}(s) \\ H_{yx(s)} & H_{yy}(s) \end{bmatrix} \begin{bmatrix} F_x(s) \\ F_y(s) \end{bmatrix} \tag{3.1}$$

3.1 System modeling

To create a model of the testbed for analysis, a simplified representation using a lumped parameter mass-spring-damper model in the mechanical domain is utilized. The model represents all moving components as lumped masses and the connections between them as parallel-connected springs and dampers. The resulting linear system, as shown in Figure 3-1, captures the dynamics of the testbed shown in Figure 2-1.

Figure 3-1 depicts a linear system that models the testbed, which includes the vibration actuation VCA, hand unit, testbed frame, FOUP, and their interconnections. The system parameters are denoted as follows: M_1 represents the centralized mass of the VCA and hand unit, k_1 and b_1 are the equivalent spring and damper coefficients, respectively, that connect the VCA to the solid ground. M_2 represents the lumped mass of the testbed frame, which can be approximated as a cantilever system, k_2 and b_2 are the corresponding lumped spring and damper coefficients, respectively, and k_3 and b_3 represent the equivalent spring and damper coefficients of the hoist cables that connect the hand unit to the frame. M_3 represents the mass of the FOUP, and k_4 and b_4 represent the equivalent spring and damper coefficients of the clamp that connects the hand unit to the FOUP. The X-component of the force from the X-axis disturbance is denoted as F_{xx}, while F_{xy} represents the X-component of the forces

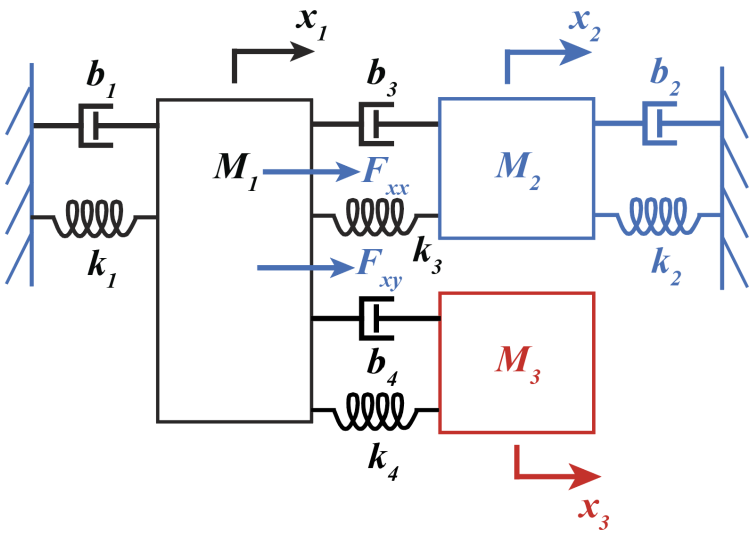

Figure 3-1: A linear mass-spring-damper model that represents the connections between the testbed, the hand unit, and the FOUP. The testbed frame is depicted in blue, the hand unit in black, and the FOUP in red. [1]

from the Y-axis disturbance.

While creating the above linear model, the following assumptions are made to simplify the system and linearize the nonlinear components. Although the resulting approximate linear model is able to capture the main system dynamics, it does possess a certain level of inaccuracy as a result of these simplifications.

1. The testbed frame is modeled as a cantilever system, and further simplified to a single mass-spring-damper system, where only the first mode related to the dominant pair of poles is considered.

2. For the sake of simplification, the dynamics of the high-stiffness stinger connecting the vibration actuation VCA and the hand unit are disregarded. Instead, the VCA and the hand unit are represented as a single mass denoted by M_1.

3. The hoist cables that connect the hand unit and the frame are modeled as a pendulum, and the small angle approximation is assumed, allowing the pendulum system to be linearized. Additionally, the elongation of the rubber-texture cables is ignored for simplification.

4. It is assumed that the clamp-equivalent spring has an unlimited stroke, so any

bumping between the clamp end and the FOUP is neglected.

5. The assumption is made that the displacement of the VCA coil is small, therefore the VCAs are considered to be linear, meaning that the output force is directly proportional to the input current.

It is important to emphasize that, the vibration of the FOUP (M_3) is caused by the motion of the OHT, which generates an acceleration on the FOUP through the force from the spring-damper system of the clamp. Therefore, the FOUP acceleration is only related to the relative displacement and velocity between the hand unit and the FOUP. In practice, it is not possible to measure the motion of the FOUP due to design limitations. Therefore, this study focuses on controlling the displacement of the hand unit using feedback control. If the vibration displacement of the hand unit is reduced, the force transmitted to the FOUP will also decrease, resulting in a reduction in FOUP vibration acceleration. The reduction can be verified by a sensor installed on the FOUP of the testbed.

3.2 System identification

This section involves identifying the testbed-hand unit-FOUP system and fitting a numerical transfer function to the measurement based on the linear model proposed in section 3.1.

First, a simplified system (the testbed-hand unit system) is identified in section 3.2.1 to verify the linear model. After that, the FOUP is added to the system in section 3.2.2, and the single-axis testbed-hand unit-FOUP system is identified, specifically for the X-axis. The Y-axis identification follows the same procedure and is not included to avoid repetition. Finally, the multi-axis testbed-hand unit-FOUP system is identified in this section. Numerical transfer functions are fitted to the measurement of every identified system based on the linear model proposed in section 3.1.

3.2.1 Testbed-hand unit system identification

The testbed-hand unit system in the X-axis can be derived as a simplified version of the model illustrated in Figure 3-1, and is depicted in Figure 3-2.

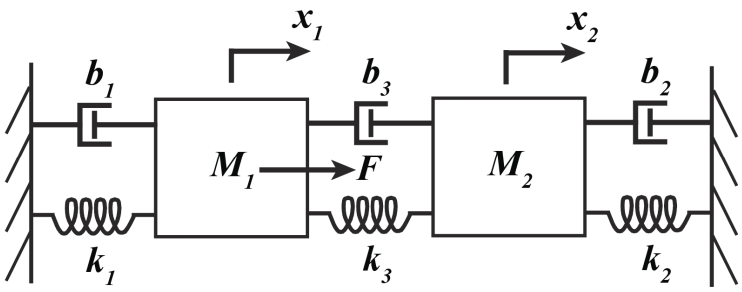

Figure 3-2: Model of the testbed-hand unit system represented by a combination of mass, spring, and damper elements. [2]

Equation (3.2) provides the analytical transfer function that relates the hand unit position x_1 to the force F.

$$\frac{X_1(s)}{F(s)} = \frac{B}{AB - (b_3 s + k_3)^2} \tag{3.2}$$

where

$$\begin{cases} A = M_1 s^2 + (b_1 + b_3)s + k_1 + k_3 \\ B = M_2 s^2 + (b_2 + b_3)s + k_2 + k_3 \end{cases}$$

To determine the numerical transfer functions appearing in Equation (3.2), a frequency sweep ranging from 0.2 Hz to 25 Hz with 0.1 Hz intervals is performed. A lock-in filter is utilized to obtain the system gain and phase at each frequency and filter out measurement noise that is uncorrelated with the inputs.

Specifically, the system is excited at each frequency (f) for 10 periods, and the product of the measurement and the sine wave ($x(t)\sin(2\pi ft)$) and the product of the measurement and the cosine wave ($x(t)\cos(2\pi ft)$) are calculated and integrated. These values correspond to the real and imaginary parts of the transfer function at that frequency. The mathematical expressions for the calculation of these values are given by Equations (3.3) and (3.4), where $|x|$ represents the amplitude of the displacement measurement, and ϕ represents the phase of the displacement.

$$\begin{aligned}\frac{1}{10T}\int_0^{10T} x(t)\sin(2\pi ft)dt &= \frac{1}{T}\int_0^{T} |x|\sin(2\pi ft+\phi)\sin(2\pi ft)dt \\ &= \frac{|x|}{2T}\int_0^{T}[\cos(\phi)-\cos(4\pi ft+\phi)]dt \\ &= \frac{|x|\cos(\phi)}{2}\end{aligned} \tag{3.3}$$

$$\begin{aligned}\frac{1}{10T}\int_0^{10T} x(t)\cos(2\pi ft)dt &= \frac{1}{T}\int_0^{T} |x|\sin(2\pi ft+\phi)\cos(2\pi ft)dt \\ &= \frac{|x|}{2T}\int_0^{T}[\sin(4\pi ft+\phi)+\sin(\phi)]dt \\ &= \frac{|x|\sin(\phi)}{2}\end{aligned} \tag{3.4}$$

To ensure that assumption 3 of small angle approximation of the hoist cables remains valid, the displacement of the hand unit is limited to a small amplitude of 200 μm during the frequency sweep. Therefore, the amplitude of the input sine current needs to be adjusted with different sweeping frequencies. Hence, the input current amplitude $I[k]$ is reduced by a certain ratio ratio$[k]$ when the sweeping frequency $f[k]$ is approaching the resonant region to prevent large displacement amplitudes.

Specifically, At each frequency $f[k]$ during the sweep, the input current amplitude is determined using Equation (3.5). After 10 periods, the lock-in filter obtains the measured gain $|H_{\text{measured}}[k]|$ and phase $\angle H_{\text{measured}}[k]$. The real gain and phase of the system at frequency $f[k]$ can then be determined using Equation (3.6). Since the frequency sweep interval is small (0.1 Hz), it is assumed that the difference between the amplitudes $|H[k+1]|$ and $|H[k]|$ is not significant. Therefore, the appropriate ratio for the next frequency $f[k+1]$ can be calculated using Equation (3.7).

$$I[k] = \frac{I[0]}{\text{ratio}[k]} \tag{3.5}$$

$$|H_{\text{real}}[k]| = \text{ratio}[k]|H_{\text{measured}}[k]|, \quad \angle H_{\text{real}}[k] = \angle H_{\text{measured}}[k] \tag{3.6}$$

$$\text{ratio}[k+1] = \frac{|H_{\text{real}}[k]|}{|H_{\text{real}}[0]|} \tag{3.7}$$

The measured bode plot between the input force (F) and the hand unit displacement (x_1) is plotted in Figure 3-3 as red dots. Besides, a numerical transfer function is fitted to the measurement based on the parametric expression in Equation (3.2) using the Python *SciPy* package. To achieve this, the logarithmic parametric equation is fitted to the logarithmic value of the measured magnitude with the method "Trust Region Reflective". The resulting fitted model is also plotted in Figure 3-3 as the black curve. The resulting linear transfer function is expressed in Equation (3.8).

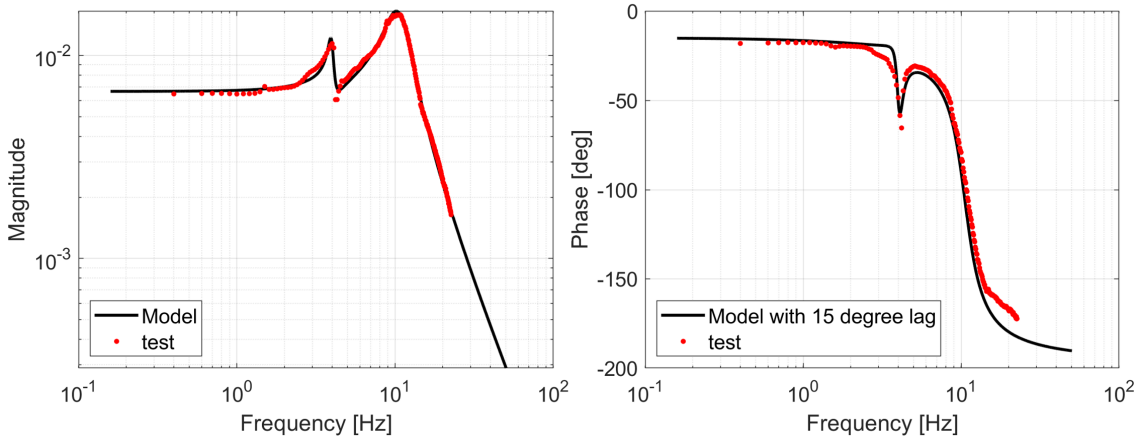

Figure 3-3: Bode plot of the testbed-hand unit system between the input force $F(s)$ and the displacement $X_1(s)$. The red dots represent the measured data, and the black curve represents the fitted model. To better match the measured phase, an additional 15° lag is added to the linear model phase. [2]

$$\frac{X_1(s)}{F(s)} = \frac{27.76(s^2 + 3.23s + 661.9)}{(s^2 + 2.18s + 626.4)(s^2 + 25.55s + 4411)} \tag{3.8}$$

Figure 3-3 shows that the fitted model magnitude curve aligns well with the experimental data. Two resonant peaks at 4 Hz and 10.8 Hz are observed in the experimental data, which correspond to two pairs of conjugated complex poles on the denominator of the numerical model Equation (3.8). Additionally, the measured anti-peak at 4.2 Hz matches the pair of conjugated complex zeros on the numerator. However, the measurement has a certain phase lag compared to the fitted linear model. This

discrepancy is caused by the friction in the linear bearing used for the VCA coil alignment. After lubricating the linear bearing, the phase lag is reduced but still exists.

To verify the accuracy of the fitted linear model, a disturbance force profile is applied to the vibration actuation actuator (VCA), and the resulting displacement of the hand unit is measured. The transfer function from the input force F to the hand unit displacement x_1, as shown in Equation (3.8), is implemented and simulated in Matlab Simulink. The same disturbance force profile is input to the linear transfer function block, and the resulting simulated displacement is plotted alongside the measurement in Figure 3-4. By comparing the simulated and measured displacement profiles, the accuracy of the fitted linear model can be evaluated.

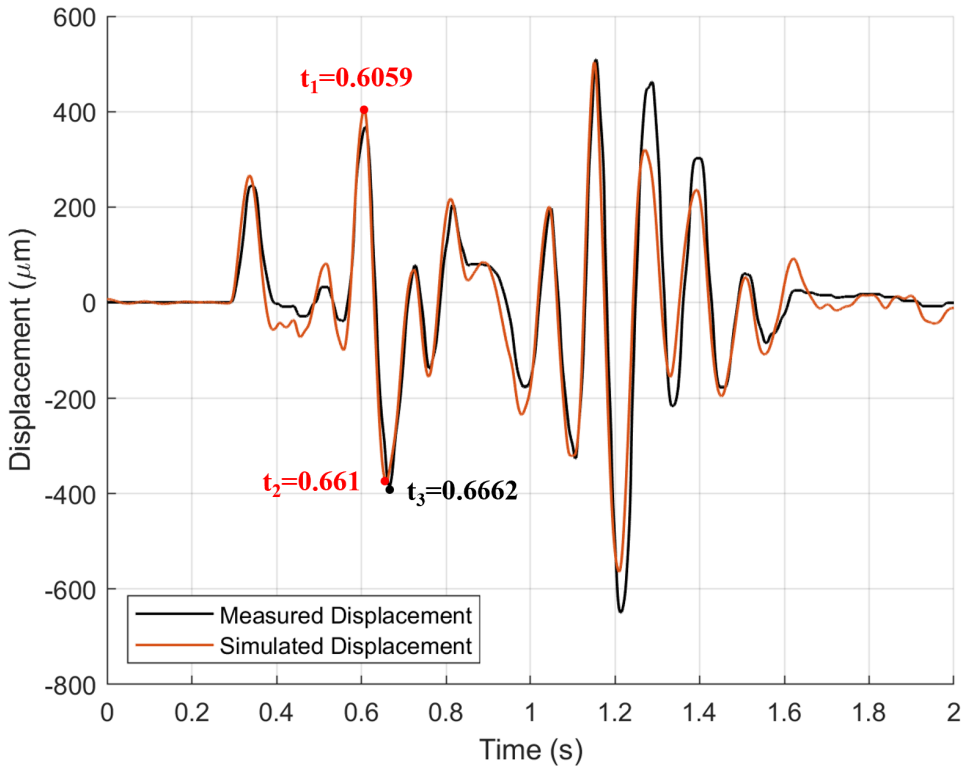

Figure 3-4: Single-axis testbed-hand unit system model verification. The measured displacement signal is compared with the Simulink simulation result. The black curve represents the measured displacement of the hand unit in response to a pre-designed force input, while the red curve shows the simulation result obtained from Simulink with the same force profile input. The time at which the peaks near 0.66s occur are labeled in the plot. [2]

The comparison between the simulated and measured displacement signals in Figure 3-4 indicates a reasonable agreement. The peaks of the simulated displacement signal are consistently observed to occur earlier than those of the measured signal, which is consistent with the measurement phase lag observed in Figure 3-3. To verify this measurement phase lag (or the model phase lead), the model phase lead of the peaks near 0.66s is calculated for verification. The time of the peaks in the simulated displacement signal (t_1 and t_2) and the time of the second peak in the measured signal (t_3) are labeled in Figure 3-4. The phase lead of the model is calculated using Equations (3.9) and (3.10). The calculated phase lead of 16.98° agrees well with the estimated 15° phase lead observed in the right plot of Figure 3-3.

$$\omega = \frac{\pi}{t_2 - t_1} = 57.02 \text{ [rad/s]} \tag{3.9}$$

$$\text{model lead} = \omega(t_3 - t_2) = 0.296 \text{ [rad]} = 16.98^\circ \tag{3.10}$$

Even though the identified linear model is not perfect and the real system contains some non-linear components, the model still manages to capture the main behavior of the system. Based on this linear model, the controller algorithm will be designed.

3.2.2 Testbed-hand unit-FOUP system identification

In this section, the system is expanded to include the FOUP, and the transfer function describing the relationship between the disturbance force F_{xx} and the position of the hand unit x_1 is determined. Figure 3-1 is used to derive the transfer function, which is presented as Equation (3.11).

$$\frac{X_1(s)}{F_{xx}(s)} = \frac{BC}{ABC - (b_3 s + k_3)^2 - (b_4 s + k_4)^2} \tag{3.11}$$

where

$$\begin{cases} A = M_1 s^2 + (b_1 + b_3 + b_4)s + k_1 + k_3 + k_4 \\ B = M_2 s^2 + (b_2 + b_3)s + k_2 + k_3 \\ C = M_3 s^2 + b_4 s + k_4 \end{cases}$$

Single-axis system identification

To identify the testbed-hand unit-FOUP system H_{xx} shown in Equation (3.1) when the Y-axis vibration actuator is disconnected, a frequency sweep is conducted from 0.2 Hz to 15 Hz with an interval of 0.1 Hz. The input force F_{xx} and the displacement output x are processed using a Lock-in amplifier to obtain the magnitude and phase of the system at each frequency and to filter out measurement noise, as specified in section 3.2.1. A numerical transfer function is then fitted to the measurement using the parametric expression in Equation (3.11) using the Python *SciPy* package. To achieve this, the logarithmic parametric equation is fitted to the logarithmic value of the measured magnitude with the method "Trust Region Reflective". The fitted model and the measurement results are plotted in Figure 3-5 for comparison.

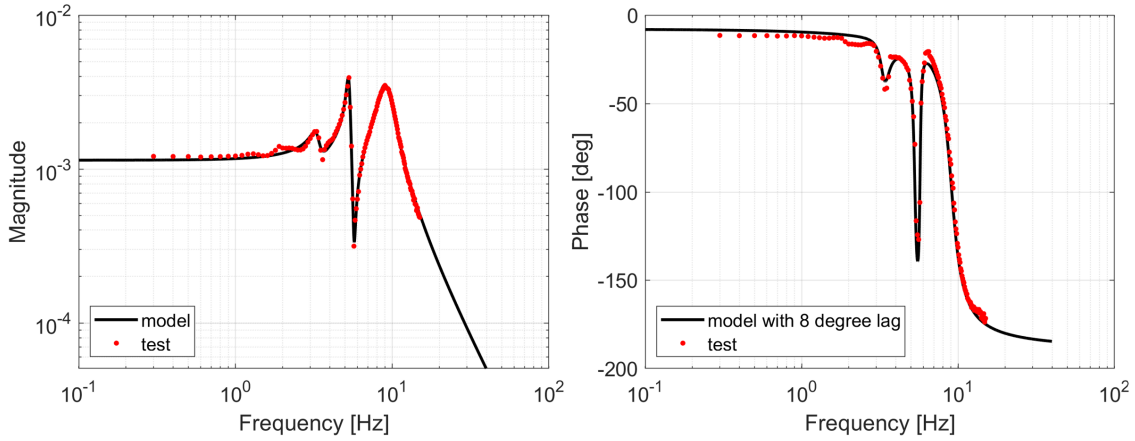

Figure 3-5: Bode plot of the single-X-axis testbed-hand unit-FOUP system between the input force $F_{xx}(s)$ and the displacement $X(s)$. The red dots represent the measured data, and the black curve represents the fitted model. To better match the measured phase, an additional 8° lag is added to the linear model phase. [1]

Figure 3-5 illustrates the system's Bode plot, which shows three resonant peaks at frequencies of 3.2 Hz, 5.3 Hz, and 9 Hz, as well as two anti-resonant peaks at 3.6 Hz and 5.7 Hz. These findings are consistent with the linear model described in Equation (3.11), which includes two pairs of conjugated complex zeros on the numerator and three pairs of conjugated complex poles on the denominator.

The fitting algorithm used for the analysis tends to disregard the first resonant and anti-resonant peaks to focus on the primary dynamics that emerge after 4 Hz to

minimize errors. However, in section 3.2.1, it is shown that the system without the FOUP has resonant and anti-resonant peaks at 4 Hz and 4.2 Hz. Therefore, when the FOUP is added to the system as an extra mass, it is expected that these resonant and anti-resonant peaks will shift slightly to a lower frequency. Consequently, the magnitude features at 3.2 Hz and 3.6 Hz, respectively, should not be ignored, as they represent the expected peaks.

The resonant and anti-resonant peaks at 3.2 Hz and 3.6 Hz will not be captured by the previous fitting algorithm, so a new approach is taken. The complex conjugate poles and zeros in the parametric model are expressed as $(s^2 + 2as + \omega_P^2 + 2a^2)$, where a and ω_P are the parameters to be fitted. a represents the damping ratio ζ multiplied by the natural frequency ω_n, and ω_P represents the resonant or anti-resonant frequency. To ensure reasonable fitting results, upper and lower boundaries are set for the parameters. ω_P is given a boundary of ± 2 Hz around the measured peak frequency, while a is set to be in the range of $[0, \infty]$. The fitted numerical transfer function is shown in Equation (3.12).

$$\frac{X(s)}{F_{xx}(s)} = \frac{3.02(s^2 + 3.69s + 465.1)(s^2 + 1.3s + 1289)}{(s^2 + 3.2s + 438)(s^2 + 2s + 1109)(s^2 + 14s + 3253)} \tag{3.12}$$

The comparison of the fitted linear model with the measurement results in Figure 3-5 reveals that the linear model has a phase lead of around 8° in comparison to the measurement. This is, again, caused by the friction in the linear bearing.

To verify the accuracy of the fitted linear model, the pre-designed disturbance force profile is applied to the VCA, and the resulting displacement of the hand unit is measured. The transfer function from the input force F_{xx} to the hand unit displacement x, as shown in Equation (3.12), is implemented and simulated in Matlab Simulink. The same disturbance force profile is input to the linear transfer function block, and the resulting simulated displacement is plotted alongside the measurement in Figure 3-6.

The comparison between the simulated and measured displacement signals in Figure 3-6 indicates a reasonable agreement. The peaks of the simulated displacement

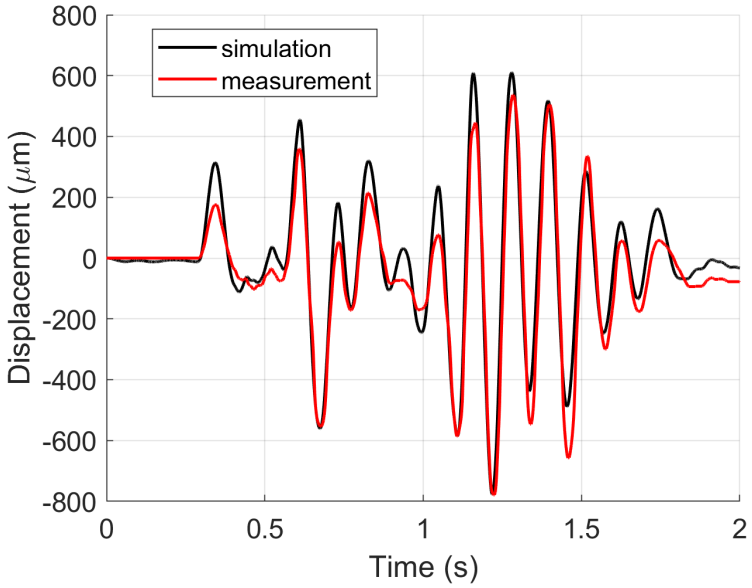

Figure 3-6: Single-axis testbed-hand unit-FOUP system model verification. The measured displacement signal is compared with the Simulink simulation result. The black curve represents the simulation result obtained from Simulink with the pre-designed force input, while the red curve shows the measured displacement of the hand unit in response to the same force profile input. [1]

signal are consistently observed to occur earlier than those of the measured signal, which is consistent with the measurement phase lag observed in Figure 3-5. Even though the identified linear model is not perfect and the real system contains some non-linear components, the model still manages to capture the main behavior of the system. Based on this linear model, the controller algorithm will be designed.

Multi-axis system identification

An identical approach is followed to determine the transfer functions between the X (or Y)-axis input force F_x (or F_y) and X (or Y)-axis hand unit displacement x (or y) in the multi-axis system. This section shows the procedure for determining the transfer function between F_x and x. In this system, both X-axis and Y-axis vibration actuators are connected to the hand unit with stingers, which changes the stiffness and damping of the connection between the hand unit and the testbed, thus the resulting system is different from the single-axis one.

A frequency sweep is performed with a similar technique (from 0.2 Hz to 15 Hz

with 0.1 Hz interval) to generate the Bode plot, as plotted in Figure 3-7.

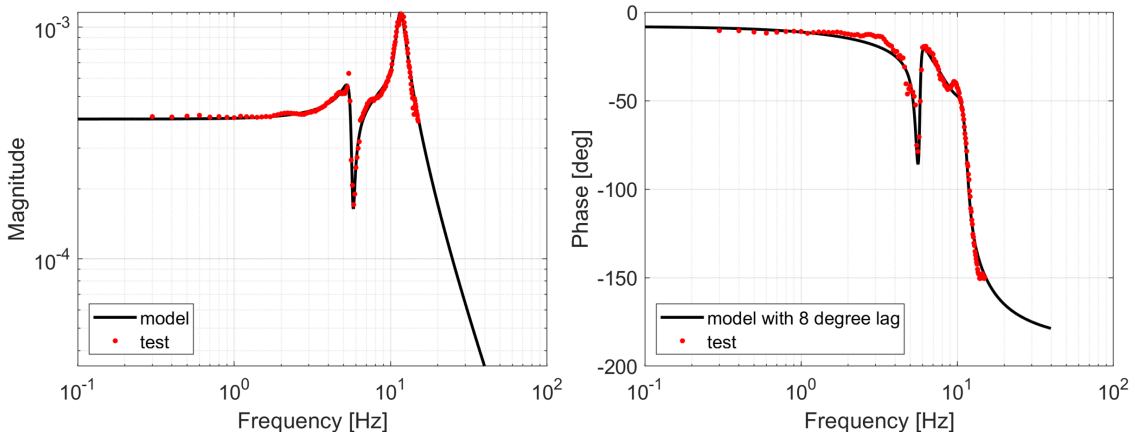

Figure 3-7: Bode plot of the multi-axis testbed-hand unit-FOUP system between the input force $F_x(s)$ and the displacement $X(s)$. The red dots represent the measured data, and the black curve represents the fitted model. To better match the measured phase, an additional 8° lag is added to the linear model phase. [1]

In Figure 3-7, one resonant peak and one anti-resonant peak vanish when compared to the single-X-axis system. This disappearance can be attributed to the fact that the Y-axis stinger and vibration actuation VCA act as a parallel spring and damper system that limits the motion of the hand unit, modifying k_3 and b_3, and thus damping the corresponding resonance and anti-resonant peaks. The transfer function fitted using the same procedure as before is also plotted in Figure 3-7 and given in Equation (3.13).

$$\frac{X(s)}{F_x(s)} = \frac{2.00(s^2 + 1.54s + 1305)(s^2 + 19.2s + 4633)}{(s^2 + 3.5s + 1219)(s^2 + 11s + 5197)(s^2 + 45s + 4766)} \tag{3.13}$$

The same procedure is applied here to verify the accuracy of the fitted linear model. The resulting simulated displacement is plotted alongside the measurement in Figure 3-8.

The comparison between the simulated and measured displacement signals in Figure 3-8 indicates a reasonable agreement. The peaks of the simulated displacement signal are consistently observed to occur earlier than those of the measured signal, which is consistent with the model's phase lead observed in Figure 3-7. Even though the identified linear model is not perfect and the real system contains some non-linear

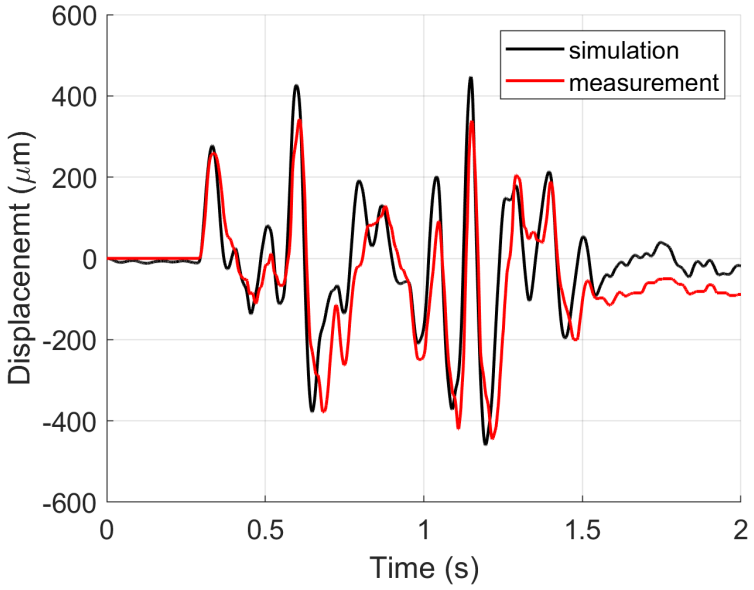

Figure 3-8: Multi-axis testbed-hand unit-FOUP system model verification. The measured displacement signal is compared with the Simulink simulation result. The black curve represents the simulation result obtained from Simulink with the pre-designed force input, while the red curve shows the measured displacement of the hand unit in response to the same force profile input. [1]

components, the model still manages to capture the main behavior of the system. Based on this linear model, the controller algorithm will be designed.

3.3 Disturbance force generation

The objective of this section is to design a vibration generation VCA input current profile to reproduce the acceleration of the hand unit observed from the actual systems running in the Samsung plants. The current profile will operate in an open loop on the vibration generation testbed, allowing the suppression system to compensate for the vibration. Therefore, the primary goal of this task is to generate a suitable current profile that will cause the desired acceleration of the hand unit when the vibration suppression system is not in use.

With the repeatable nature of the vibration generation testbed (the same input will result in the same output), an iterative learning controller is first investigated to directly control the hand unit acceleration. The controller consists of two parts: a

feedforward controller that is updated in each iteration and a feedback controller with low gains. The block diagram is shown in Figure 3-9, where a_{ref} is the acceleration reference to be followed, i_k and i_{k+1} are the control efforts of the k^{th} and $k+1^{th}$ iteration, a is the hand unit acceleration, and block H represents the measurement dynamics of the accelerometer. The dynamic of the plant between the input force F (which is proportional to the input current) and the hand unit acceleration a is shown in Equation (3.14), which is derived by differentiating Equation (3.8) twice.

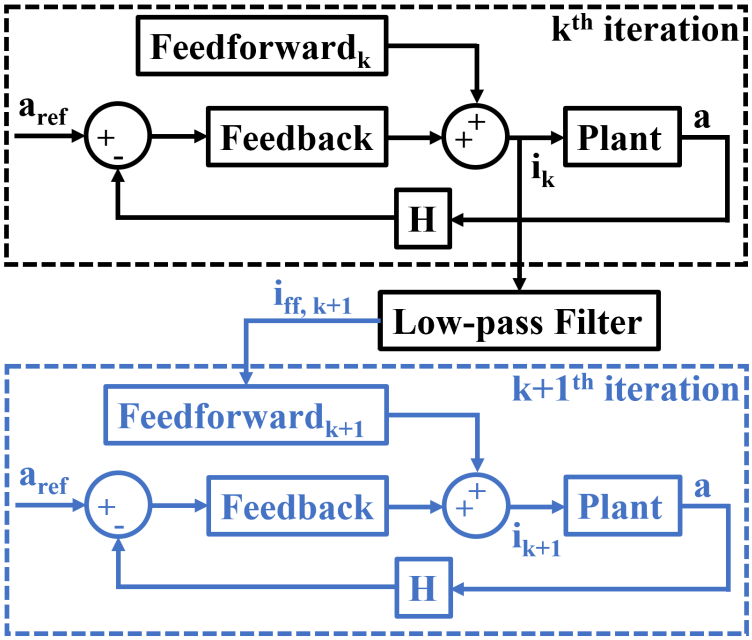

Figure 3-9: Block diagram of the iterative learning acceleration controller.

$$\frac{A(s)}{I(s)} = \frac{27.76(s^2 + 3.23s + 661.9)s^2}{(s^2 + 2.18s + 626.4)(s^2 + 25.55s + 4411)} \tag{3.14}$$

Equation (3.14) shows that the system being controlled has the same number of poles and zeros for the dynamic between the input force and the hand unit acceleration, which is not strictly proper. This non-ideal characteristic, along with sensor error and hardware delay, means that a high feedback gain would generate high-frequency oscillations. Thus, a low feedback gain is used, but it still tries to reduce the error between the measured acceleration and the reference during each iteration. As a result, the controlled acceleration from both the feedforward and feedback con-

trollers is closer to the reference acceleration than the acceleration obtained from the feedforward controller alone. Therefore, the method used for iterating is that, after the k^{th} iteration, the control effort (i_k) obtained is smoothed using a low-pass filter to reduce high-frequency components, and then this smoothed time profile is utilized as the feedforward part ($i_{ff,k+1}$) of the $k+1^{th}$ iteration. Figure 3-10 shows the iterative learning result. Since the generation of feedforward current passes a low-pass filter, and the feedback gain is small, it can be noticed in Figure 3-10 that the high-frequency component of the reference is not matched. Despite the high-frequency mismatch, many of the acceleration high peaks are reached, which can be used for vibration suppression control. The control effort (current) was input to the vibration actuation VCA in an open loop during the later vibration control section.

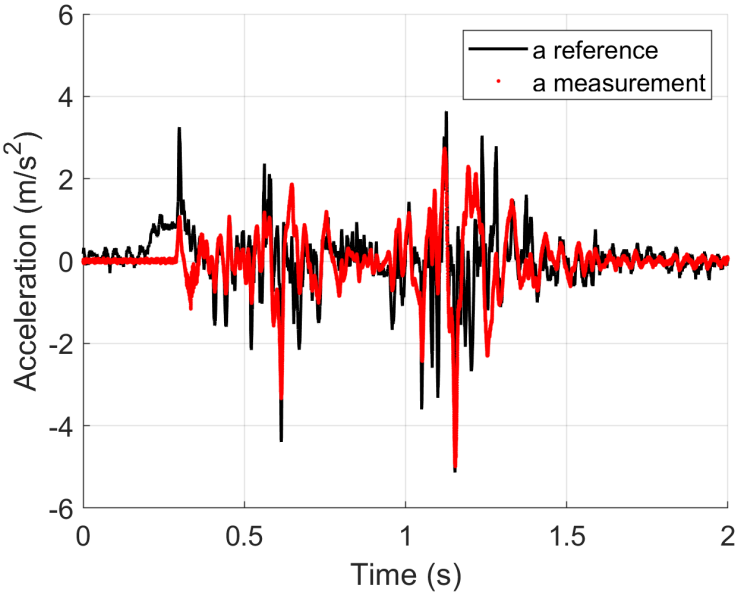

Figure 3-10: Comparison of the acceleration reference collected from the hand unit in the Samsung plant (black) and the result obtained from the iterative learning (red). [2]

3.4 Summary

This chapter focuses on system modeling and identification. The approach begins by linearizing the dominant dynamic of the system using a lumped parameter model,

and deriving a transfer function. Next, the magnitude and phase of the system are measured under different frequencies, and numerical transfer functions are fitted to the data. Finally, a current input profile is generated to simulate the vibration observed from the hand unit used in Samsung's facilities.

Given the complexity of the multi-axis testbed-hand unit-FOUP system, the analysis starts with a simplified version of the system, which is the testbed-hand unit system in the X-axis direction, and progresses by introducing additional complexities such as clamping the FOUP beneath the hand unit and adding the Y-axis vibration actuator. This gradual approach provides a better understanding of the system dynamics and results in more accurate modeling and identification.

Chapter 4

Active Vibration Suppression Controller Design and Experimental Result

In this chapter, the design process of the control algorithm aimed at suppressing the vibration displacement of the hand unit and the vibration acceleration of the FOUP is presented. First, section 4.1 shows a comprehensive analysis of the vibration signal characteristic that is to be suppressed. Based on the analysis, the appropriate type of control technique to be employed is selected.

Next, the controller for the vibration suppression task is designed. Due to the complexity of the multi-axis testbed-hand unit-FOUP system, a systematic approach is employed to follow the process in chapter 3 and to develop the solution by gradually increasing the complexity of the system. First in section 4.2, different controllers (PID and DOBC) are designed for the hand unit displacement control of the testbed-hand unit system, and are tested on the hardware. The performance of the PID controller and the DOBC are compared in this section, and DOBC is selected as the preferred option due to its superior performance. Next in section 4.3, the FOUP is added to the system and DOBC is developed for the FOUP vibration acceleration suppression task. A DOBC is first designed for the single-axis testbed-hand unit-FOUP system and tested on the hardware. The performance proves that the hand unit displacement

control facilitates the FOUP vibration suppression, and the DOBC can observe the main feature of the disturbance in the designed direction. Next, two DOBCs are developed for the X and Y axes of the multi-axis testbed-hand unit-FOUP system and tested on the hardware. The test results show that the DOBCs can successfully suppress vibrations in the coupled multi-axis system when disturbances are applied simultaneously.

4.1 Determine the controller structure

The initial controller candidates being considered include:

1. Proportional integral derivative (PID)
2. Disturbance Observer-Based Controller (DOBC)
3. Repetitive control
4. Iterative learning control
5. Data-driven learning

The PID controller is chosen as the benchmark solution as an initial starting point. The DOBC is selected as the primary algorithm to treat the vibration force input as a disturbance rejection problem. As confirmed in chapter 3.2, the system is mainly linear without significant nonlinearities from the system identification. This feature is advantageous for implementing the DOBC, which is therefore chosen for this problem.

The remaining algorithms can only be effective for specific situations where the vibration signal to be suppressed has specific properties. After a thorough analysis of the vibration signal from the measurement data collected at the factory plant, it has been concluded that the remaining algorithms are not appropriate for this specific application. The vibration data does not exhibit any dominant frequency components and instead spans the entire frequency range. Hence, the repetitive control technique is not suitable for this application. The time domain acceleration profiles of each test

from the Samsung plant are distinct due to the different initial conditions and the different disturbance sources such as gaps on the track and motion changes of the OHT vehicles. This makes it difficult to apply iterative learning control. While the data-driven learning algorithm remains a potential option for future exploration, it would require a significant number of datasets from the OHT hand unit in the factory.

When designing the controller, it is necessary to take into account the practical limitations of the hardware transducer. The main constraint of our controller hardware is the limited force and stroke of the controller VCA.

1. The limited force makes it impossible to have arbitrarily high controller gain and restricts the settling time of the controlled signal.

2. The limited stroke, as illustrated in Figure 4-1, is a potential extra-disturbance source that can exacerbate the vibration problem. If the VCA moving mass reaches the stroke limit and thus hits the hand unit, the impact will cause an extra sharp vibration peak.

Thus, it is crucial to consider these practical limits during controller design to ensure that the controller can effectively suppress vibrations while operating within the constraints of the hardware.

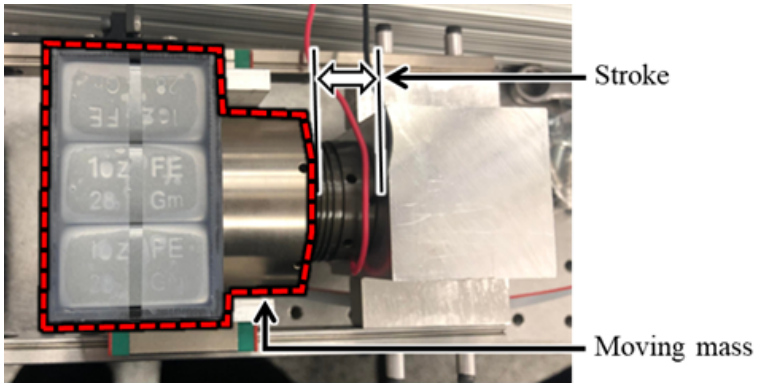

Figure 4-1: The limited stroke of the vibration control VCA. [2]

To ensure effective vibration suppression, there are two primary tasks to be accomplished in the design of the vibration suppression controller:

1. to actuate the controller VCA moving mass to generate inertia force, and

2. to keep the controller VCA moving mass within a certain range to prevent additional disturbances caused by the moving mass reaching its movement limit.

The baseline PID controller consists of a Proportional-Integral (PI) controller that is used to control the displacement of the hand unit, and another PI controller that is used to control the displacement of the controller VCA moving mass. In this thesis, it is also called the double PI controller in this thesis.

In the case of the Disturbance Observer-Based Controller (DOBC), the designed controller structure is illustrated in Figure 4-2. A disturbance observer is implemented to estimate and suppress the majority of the real-time disturbance. In addition, the same double PI controller used in the baseline PID controller for hand unit displacement control and for controlling the VCA moving mass displacement is also implemented in the DOBC.

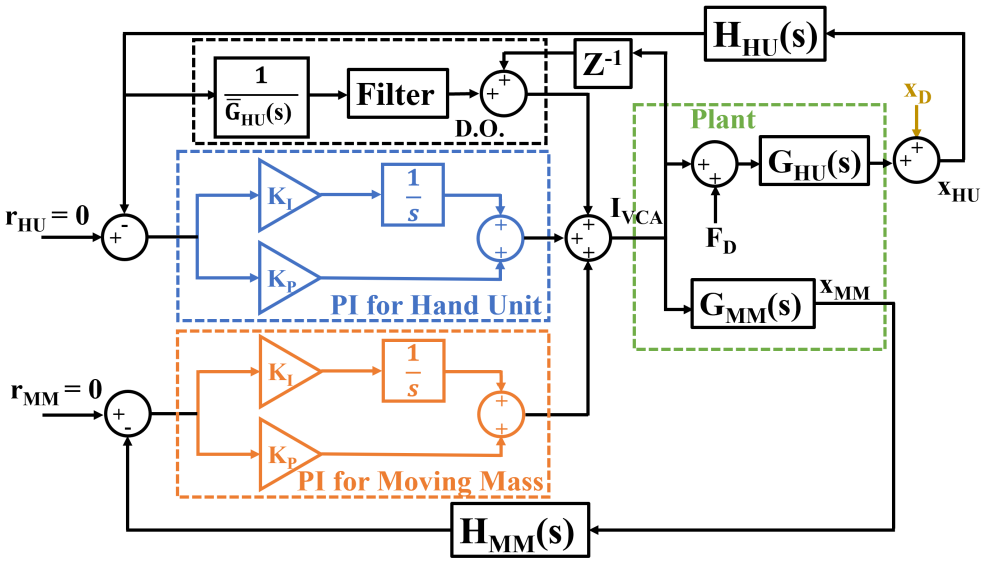

Figure 4-2: Block diagram of the controller structure. [1]

The parameters shown in Figure 4-2 are:

1. r_{HU} and r_{MM} are the reference value of the hand unit displacement and vibration control VCA moving mass displacement. During operation, both are set to 0.

2. $G_{\mathrm{HU}}(s)$ and $G_{\mathrm{MM}}(s)$ are the transfer function between the vibration control VCA input current and the hand unit displacement, and the transfer function

between the input current and the VCA moving mass displacement.

3. $H_{\mathrm{HU}}(s)$ and $H_{\mathrm{MM}}(s)$ are the dynamic of the measurement of the hand unit displacement and the VCA moving mass displacement.

4. The $\frac{1}{\bar{G}_{\mathrm{HU}(s)}}$ and the filter block (denoted as D.O. in Figure 4-2) represent the disturbance observer, where $\bar{G}_{\mathrm{HU}}(s)$ is the modified version of $G_{\mathrm{HU}}(s)$ and the filter is the low-pass filter used to stabilize the output, which will be elaborated in section 4.2.2.

It is important to note that the observed disturbance in the current iteration is the result of the sum of the disturbance and the control effort from the previous iteration. Therefore, to effectively suppress the disturbance in the current iteration, the control effort from the previous iteration needs to be added. It should also be noted that assumption 5 assumes linearity of the VCA. Therefore, the input current of the vibration control VCA is proportional to the inertia force. Additionally, under assumption 2, the hand unit and the vibration actuation VCA are lumped as one mass. Consequently, the transfer function $G_{\mathrm{HU}}(s)$ is the same as the transfer function identified in section 3.2, but with an additional constant gain resulting from the VCA force constant.

4.2 Testbed-hand unit system control

In this section, the design of the baseline PID controller is developed based on the mentioned structure. The developed PID controller is simulated in Simulink, and implemented on the hardware. Next, the DOBC is designed and implemented on the hardware. Finally, a performance comparison between the two controllers is conducted in this section.

4.2.1 PID controller

The baseline PID controller consists of two PI controllers, one for hand unit displacement control and the other for the controller VCA moving mass displacement control.

Each PI controller is composed of a proportional gain and an integral term, which operate on the difference between the reference and the measurement. The proportional gain increases the speed of convergence, while the integral gain eliminates the steady-state error.

The proportional gain and the integral gain are tuned for the best performance. The hand unit displacement control PI is adjusted first by gradually increasing the gains. As the gains increase, the hand unit displacement is suppressed better, but the moving mass of the inertia force actuator (the magnet of the VCA) travels a longer distance. To prevent extra vibration caused by the impact between the moving mass and the mounting base of the VCA coil (as depicted in Figure 4-1), the PI for the moving mass displacement control is then tuned to restrict the moving mass from moving too far away from the center position. The final gains are:

$$K_{P,\mathrm{HU}} = 0.006$$

$$K_{I,\mathrm{HU}} = 0.025$$

$$K_{P,\mathrm{MM}} = 0.0002$$

$$K_{I,\mathrm{MM}} = 0$$

The performance of the baseline PID controller is evaluated both through simulation in Simulink and on the testbed. In Simulink, various input signals including step, sinusoidal, and pre-designed current profile (described in section 3.3) are used to test the controller performance. On the testbed, the pre-designed current profile is tested.

In Simulink, a step response is first tested and the result is shown in Figure 4-3(a). Then, three sinusoidal inputs at three different vibration characteristic frequencies (3 Hz, 8 Hz, and 20 Hz) are tested, and the results are shown in Figure 4-3(b)-(d).

The performance of the baseline PID controller on the hardware is shown and compared with the Simulink simulation in Figure 4-4a. The blue region in the plot represents a 30% threshold of the maximum displacement. The reduction in peak vibrations is a suitable metric for measuring the effectiveness of vibration suppres-

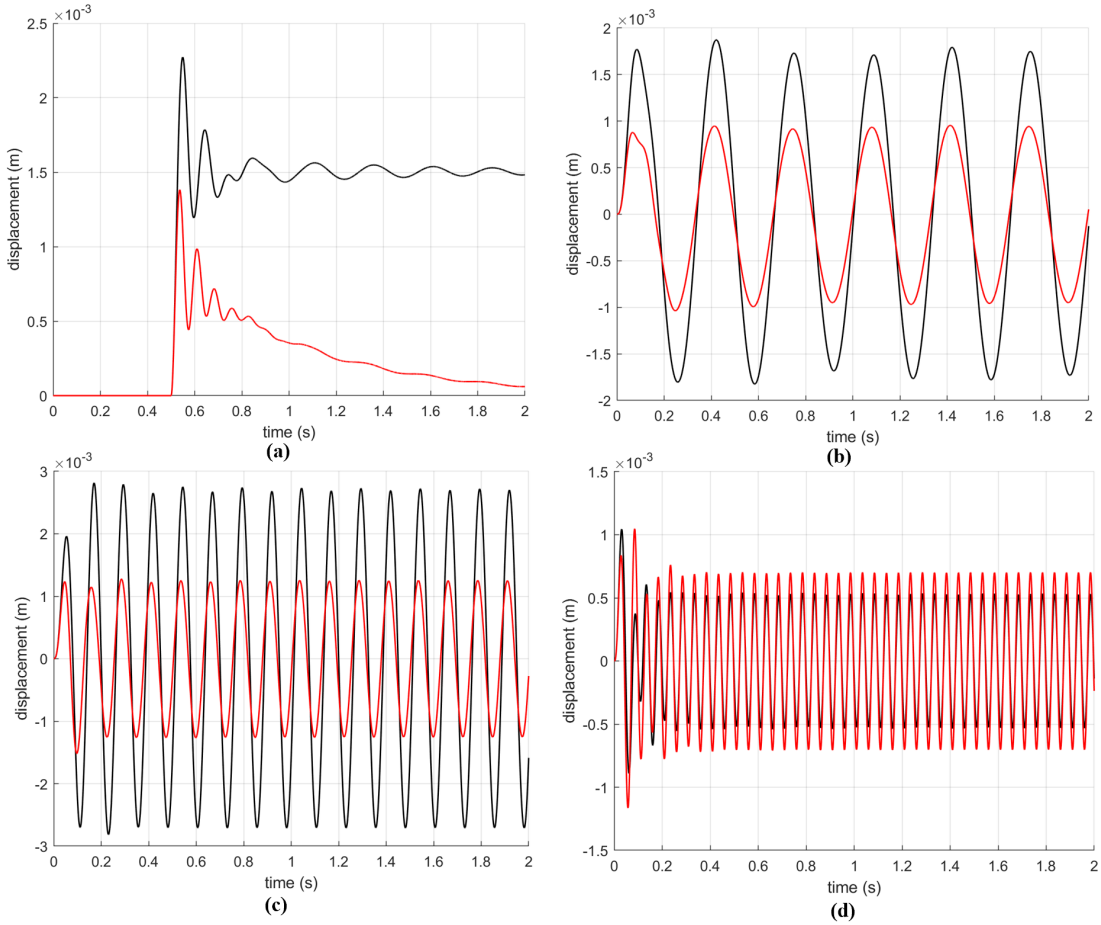

Figure 4-3: The simulation results of the baseline PID controller in Simulink. Black curves represent open loop responses, and red curves represent PI controller responses. (**a**): step response. (**b**): 3 Hz sine response. (**c**): 8 Hz sine response. (**d**): 20 Hz sine response. [2]

sion, as when the OHT vehicles are traveling, it is subjected to mostly impact-type vibrations. Thus, the ratio between the controlled displacement peaks of the hardware setup and the open loop displacement peaks is plotted in Figure 4-4b to show the suppression of the controller on the vibration peaks. Better vibration suppression performance corresponds to smaller ratios. The ratio is also summarized in Table 4.2 and compared with the results of the DOBC in section 4.2.2.

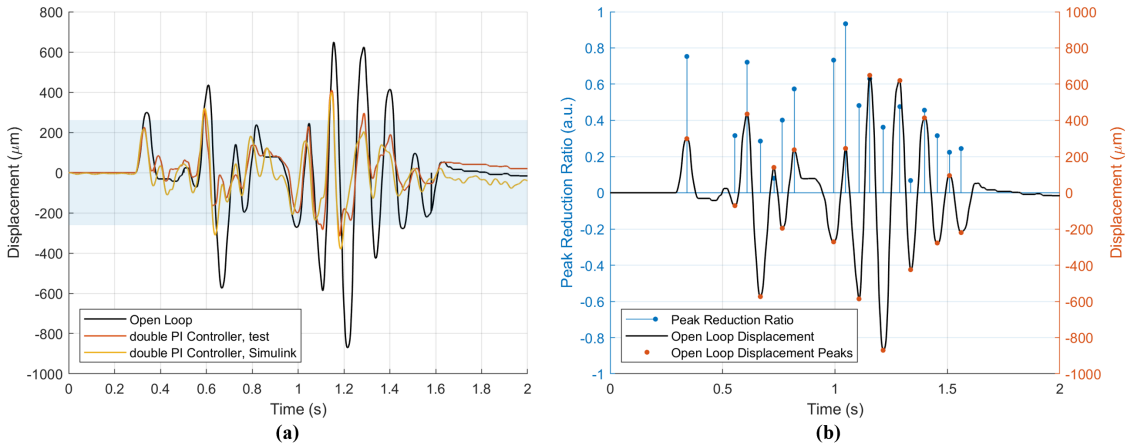

Figure 4-4: The performance of the baseline PID controller on the testbed-hand unit system: (**a**) The black curve represents the open loop displacement, the red curve represents the controlled displacement, and the yellow curve represents the simulation results. The blue rectangular region shows the 30% maximum open loop displacement threshold. (**b**) The black curve represents the open loop displacement, the red dots represent the open loop displacement peaks to be suppressed, and the blue dots represent the ratio between the controlled displacement peaks and the open loop ones. [2]

As shown in Figure 4-4(a), the Simulink result (yellow curve) closely matches the hardware measurements (red curve), confirming the accuracy of the model. The positive peak is dropping from 648.75 μm to 408.75 μm. The negative peak is reduced from -870 μm to -315 μm. However, some displacement peaks controlled by the PID controller still exceed the 30% threshold, indicating the need for a more effective control algorithm.

4.2.2 Disturbance Observer-Based Controller (DOBC)

The Disturbance Observer-Based Controller is composed of three parts: a disturbance observer to estimate and suppress the majority of the real-time disturbance, a PI controller for hand unit displacement control to compensate for other types of error, and another PI controller to control the displacement of the controller VCA moving mass. The overall structure of the controller is shown in Figure 4-2.

The performance of the DOBC is expected to be better compared to the baseline PID controller. The PID controller is designed to respond to the error of the displacement signal (difference between the measured displacement and the reference), and generate an input force with the VCA to the mechanical system. However, this has a limited effect due to the lag in the mechanical system dynamics. In contrast, the disturbance observer in the DOBC estimates the real-time disturbance force and responds directly with added control effort. By demanding the inertia force actuator to output a force with the same amplitude but opposite direction as the estimated disturbance force, large displacement peaks can be attenuated more effectively.

To estimate the input force, the system transfer function Equation (3.8) is inverted and simplified by removing similar terms shown in the numerator and denominator. To avoid the instability caused by differentiating the measurement signal and having more zeros than poles, two low-pass filters at 150 rad/s are added. The resulting transfer function of the disturbance observer (D.O.) is shown in Equation (4.1).

$$\frac{I(s)}{X(s)} = \frac{Gain_2(s^2 + 25.55s + 4411)}{(s + 150)^2} \tag{4.1}$$

To discretize the D.O. for hardware implementation, bi-linear z-transform is applied to get a discrete transfer function by substituting s to $\frac{2(z-1)}{T(z+1)}$, as shown in Equation (4.2). Since the FPGA main loop operates at a rate of 10 kHz, the sampling period is set to $T = 0.1$ ms.

$$\frac{I(z)}{X(z)} = \frac{Gain_4(400515411z^2 - 799991178z + 399493411)}{(406022500z^2 - 799955000z + 394022500)} \tag{4.2}$$

To implement the z-domain transfer function on hardware, $x[k]z^{-1} = x[k-1]$ is applied and Equation (4.2) can be rewritten as Equation (4.3). The implementation in Simulink is shown in Figure 4-5.

$$\begin{aligned} I[k] &= 1.970223I[k-1] - 0.970445I[k-2] + \text{Gain}_4(0.986436x[k] \\ &\quad -1.970312x[k-1] + 0.983919x[k-2]) \end{aligned} \tag{4.3}$$

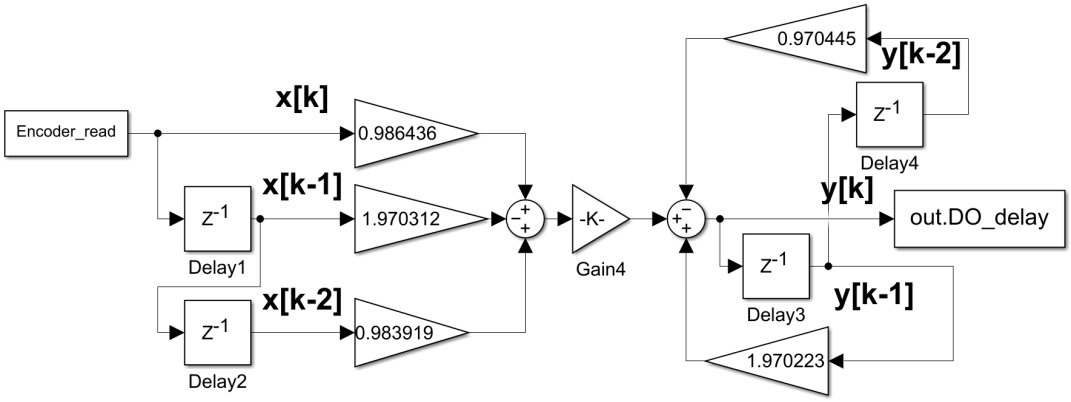

Figure 4-5: Implementation of the disturbance observer in Simulink. [2]

In Figure 4-5, the D.O. is implemented in Simulink and verified by comparing the measured disturbance with the observed disturbance. The measured disturbance is fed into both the continuous and discrete D.O. transfer function, and the resulting observed disturbance is compared with the actual input current, as shown in Figure4-6. It deserves to be noticed that the linearity of the disturbance actuation VCA is assumed, so the observed current is proportional to the observed disturbance.

As shown in Figure 4-6, the observed current closely follows the trend of the actual input current. When taking a closer look at the signal, there is a certain level of phase lag due to the implementation of the low-pass filter added for system stability. To further investigate this phenomenon, two regions of interest are selected and are zoomed in, as highlighted in Figure 4-6. The time corresponding to the two peaks of the actual input current (t_1 and t_2) and the first lagged peak of the observed current (t_3) are identified and labeled for each region. Using Equation (4.4) - (4.6),

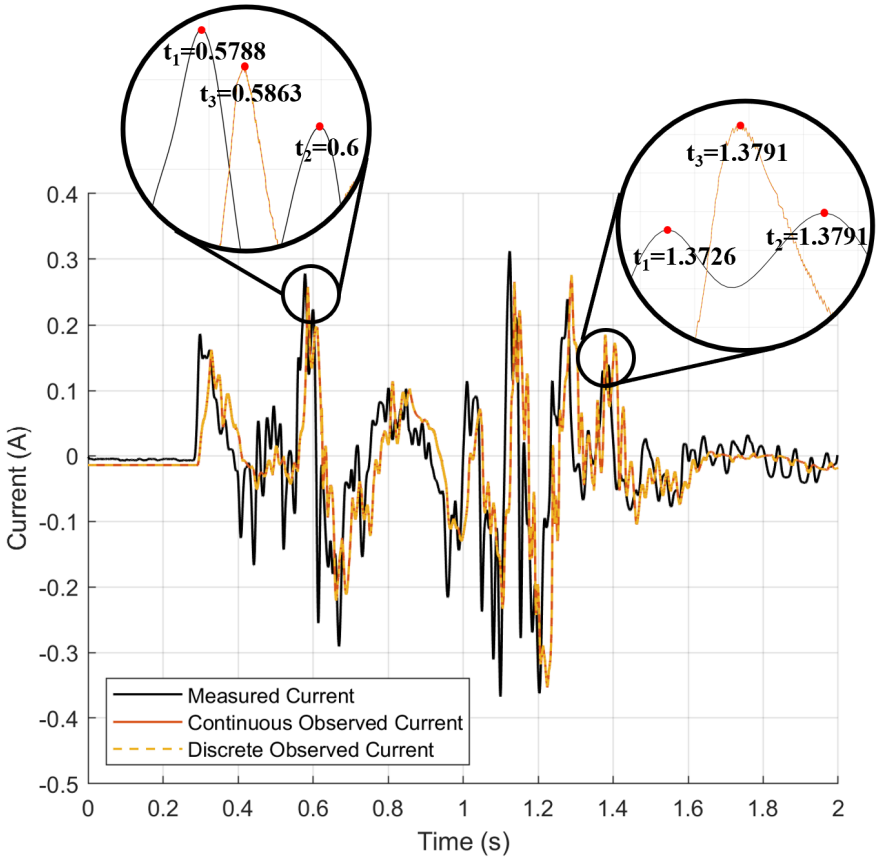

Figure 4-6: Testbed-hand unit system disturbance observer (D.O.) simulation. The black curve represents the real input current of the disturbance actuator, which is proportional to the input disturbance; the red curve represents the observed disturbance from the measured displacement with the continuous D.O.; the yellow curve represents the observed disturbance with the discrete D.O.. [2]

the phase lags are then computed and compared with the theoretical phase lag of the low-pass filter, and the results are listed in Table 4.1.

$$\omega = \frac{2\pi}{t_2 - t_1} \tag{4.4}$$

$$\text{theoretical lag} = \angle \frac{1}{(j\omega + 150)^2} \tag{4.5}$$

$$\text{measured lag} = \omega(t_3 - t_1) \tag{4.6}$$

	frequency ω [rad/s]	theoretical lag [°]	measured lag [°]
peak 1	296.5	126.3	126.9
peak 2	432.3	141.7	161

Table 4.1: Theoretical and measured phase lags of the two peaks highlighted in Figure 4-6.

After implementing the disturbance observer on the vibration suppression hardware, the double PI controller is also added in parallel to compensate for the error from the disturbance estimate to improve the performance. The performance of the disturbance observer-based controller (DOBC) is shown in Figure 4-7. The displacement is effectively suppressed and never exceeds 30% of the maximum open loop peak. The positive peak is decreased from 648.75 μm to 110 μm, while the negative peak is reduced from -870 μm to -222.5 μm. Similar to the baseline PID controller analysis, the peak ratio between the controlled displacement peaks and the open loop ones is plotted in Figure 4-7(b) to demonstrate the effectiveness of the DOBC in suppressing the vibration peaks. The results are also presented in Table 4.2, where they are compared with the PID controller performance.

4.3 Testbed-hand unit-FOUP system DOBC control

In this section, the FOUP is integrated into the system, and a Disturbance Observer-Based Controller (DOBC) is developed for the FOUP vibration acceleration suppression task. In section 4.3.1, A DOBC is first designed based on the identified

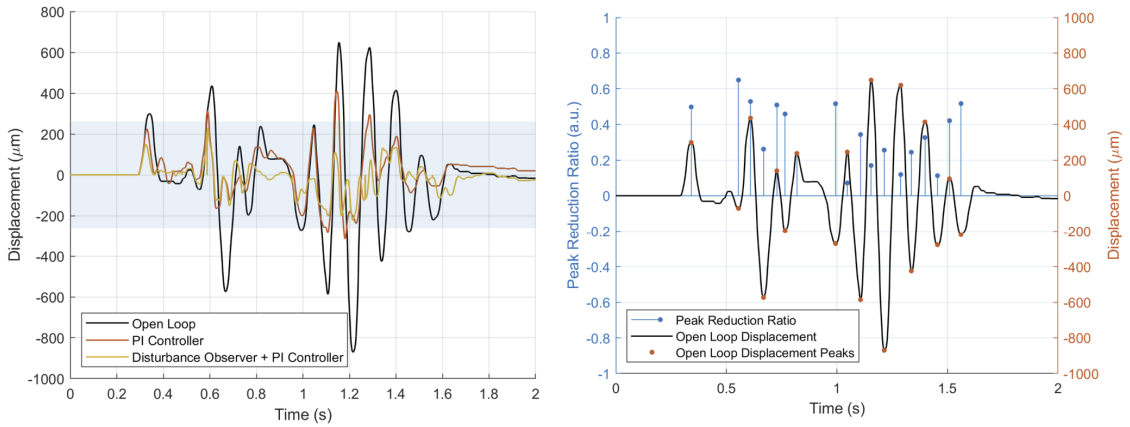

(a) (b)

Figure 4-7: The performance of the Disturbance Observer-Based Controller (DOBC) on the testbed-hand unit system. (**a**) The black curve represents the open loop displacement, the red curve represents the baseline PID controller displacement, and the yellow curve represents the DOBC displacement. The blue rectangular region shows the 30% maximum open loop displacement threshold. (**b**) The black curve represents the open loop displacement, the red dots represent the open loop displacement peaks to be suppressed, and the blue dots represent the ratio between the controlled displacement peaks and the open loop ones. [2]

Peak	Open Loop [μm]	PID [μm]	DOBC [μm]	PID Ratio	DOBC Ratio
1	298.75	225	148.75	0.753	0.498
2	-71.25	-22.5	-46.25	0.316	0.649
3	435	313.75	230	0.721	0.529
4	-573.75	-163.75	-150	0.285	0.261
5	140	-11.25	71.25	0.080	0.509
6	-196.25	-78.75	-90	0.401	0.458
7	237.5	136.25	56.25	0.574	0.237
8	-271.25	-198.75	-140	0.733	0.516
9	245	228.75	-17.5	0.934	0.071
10	-586.25	-282.5	-201.25	0.482	0.343
11	648.75	408.75	110	0.630	0.170
12	-870	-315	-222.5	0.362	0.256
13	620	295	73.75	0.476	0.119
14	-425	-28.75	-103.75	0.068	0.244
15	413.75	188.75	135	0.456	0.326
16	-277.5	-87.5	-31.25	0.315	0.113
17	95	21.25	40	0.224	0.421
18	-220	-53.75	-113.75	0.244	0.517

Table 4.2: Displacement peaks value and the peak reduction ratio of Open Loop, PID controller, and DOBC.

single-axis testbed-hand unit-FOUP system in Equation (3.12), and tested on the hardware. The result indicates that the hand unit displacement control helps the FOUP vibration suppression, and the DOBC is capable of observing the main feature of the disturbance in the designed direction. Next in section 4.3.2, two DOBCs are developed for the X and Y axes of the identified multi-axis testbed-hand unit-FOUP system in Equation (3.13), and tested on the hardware. The test results demonstrate that the DOBCs can effectively suppress vibrations in the coupled multi-axis system when disturbances are applied simultaneously.

4.3.1 Single-axis system control

This section shows the controller design for the single-axis testbed-hand unit-FOUP system. The controller's structure is the same as the one illustrated in Figure 4-2. A disturbance observer (D.O.) is first derived based on Equation (3.12), which represents the transfer function between the input force and the hand unit displacement. The same double PI controller mentioned in section 4.2.2 is added to compensate for the model error and other disturbance sources, and to control the VCA moving mass position to avoid any collision between the moving mass and the base, which is a design consideration illustrated in Figure 4-1.

To design the D.O. for the single-X-axis system, the transfer function between the input disturbance F_x and the hand unit X-axis displacement x described in Equation (3.12) is simplified and inverted. To prevent instability associated with differentiating the measurement signal and having more zeros than poles, two low-pass filters are added. The transfer function of the D.O. is shown in Equation (4.7).

$$\frac{\hat{F}_x(s)}{X(s)} = \frac{\text{Gain}_3(s^2 + 2.3s + 1109)(s^2 + 14.4s + 3234)}{(s^2 + 1.19s + 1293)(s + 80)^2} \tag{4.7}$$

The continuous D.O. transfer function Equation (4.7) is discretized for implementation in a digital control system. In this case, the *c2d* command in Matlab is used with the "Zero-Order Hold" method at a sampling frequency of 10 kHz, which is the hardware controller loop frequency on the FPGA. The resulting discrete-time transfer

function is rearranged using $x[k]z^{-1} = x[k-1]$. This yields the implementation of the discretized D.O. shown in Equation (4.8).

$$\begin{aligned} F[k] &= 3.983931656F[k-1] - 5.9518734899F[k-2] \\ &\quad +3.9519517973F[k-3] - 0.9840099642F[k-4] \\ &\quad +\text{Gain}_4(0.715853206x[k] - 2.8621849758x[k-1] \\ &\quad +4.2914668615x[k-2] - 2.8597916022x[k-3] \\ &\quad +0.7146565108x[k-4]) \end{aligned} \tag{4.8}$$

In practical implementation, it is important to use high-precision coefficients to avoid unstable estimation caused by errors from the high sampling rate and high-order observer transfer function. In this case, the Fixed-point type in LabVIEW is set to a precision of 10^{-13}, which is sufficient for the designed D.O..

The designed D.O. is evaluated first in Simulink simulation and later verified on hardware implemented in LabVIEW FPGA. With the same displacement input, the observed disturbance are plotted in Figure 4-8.

Figure 4-8 shows that the FPGA calculated disturbance has some discrepancies compared to the Simulink simulation. Despite these differences, the disturbance observer on the hardware is able to capture the main dynamics of the input disturbance. However, due to the model's simplification and the low-pass filter, the observed disturbance has some errors and phase lag compared to the real disturbance input. Note that the 64-bit fixed-point numbers on the FPGA may accumulate a certain level of error during calculations.

Using the same control structure shown in Figure 4-2 and the same controller parameters from section 4.2.2, the performance is shown in Figure 4-9.

The result in Figure 4-9 shows that the maximum peak displacement of the hand unit is reduced from 773.75 μm to 352.5 μm, and the maximum peak acceleration of the FOUP is reduced from 2.55 m/s^2 to 2.15 m/s^2. This confirms that the linear model used to represent the clamp as a parallel spring-damper system is correct, and that reducing the hand unit displacement leads to a reduction in the acceleration of

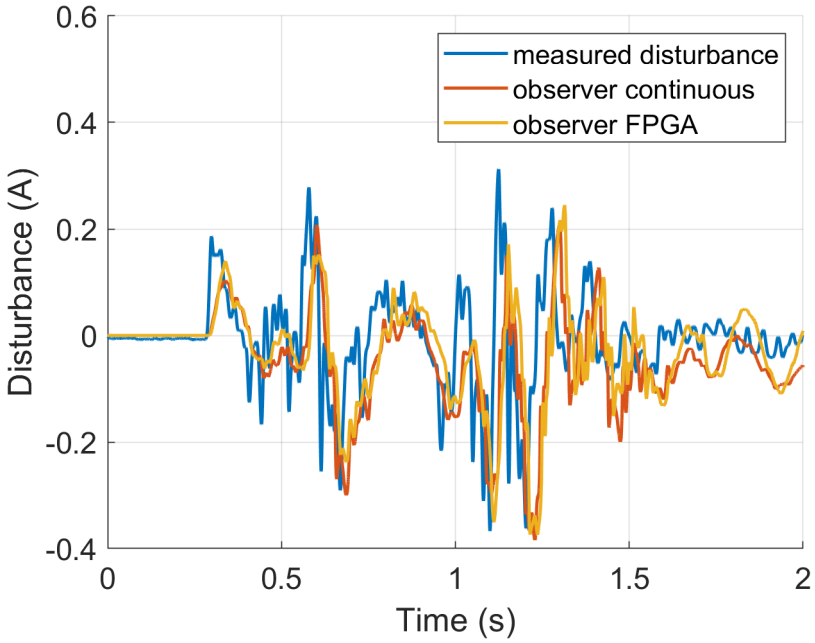

Figure 4-8: Single-axis testbed-hand unit-FOUP system disturbance observer (D.O.) simulation. The blue curve represents the real input current of the disturbance actuator, which is proportional to the input disturbance; the red curve represents the observed disturbance from the measured displacement in Simulink; the yellow curve represents the observed disturbance with the discrete D.O. on hardware FPGA. [1]

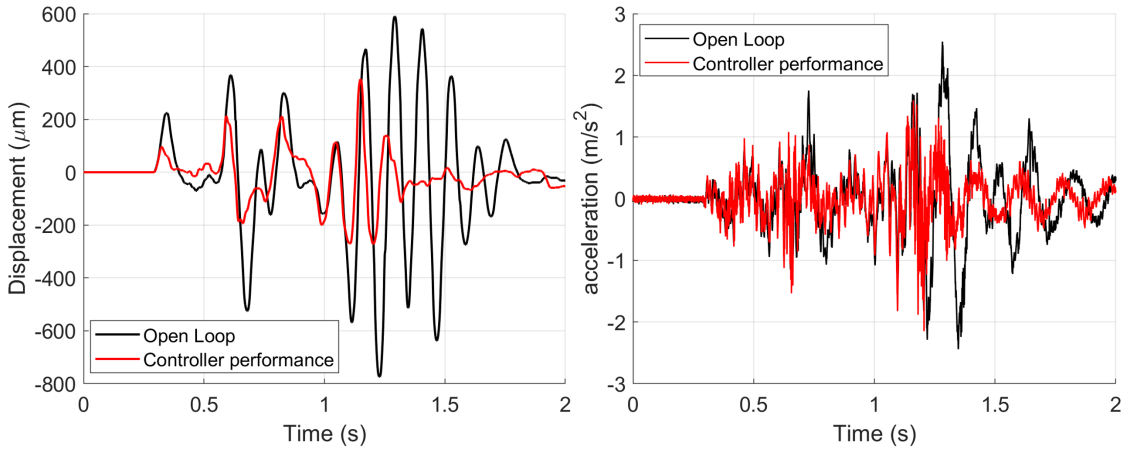

Figure 4-9: The performance of the Disturbance Observer-Based Controller (DOBC) on the single-axis testbed-hand unit-FOUP system. Left: The black curve represents the hand unit displacement in the X-axis with a designed disturbance input in the open loop, and the red curve represents that in the controlled closed loop; Right: the black curve represents the FOUP acceleration in the X-axis in the open loop, and the red curve represents that in the controlled closed loop. [1]

the FOUP vibration.

4.3.2 Multi-axis system control

The X-axis controller design for the multi-axis testbed-hand unit-FOUP system is presented in this section. The design procedure for the Y-axis controller is the same and hence, is not included to avoid repetition. The disturbance observer (D.O.) is designed based on the transfer function Equation (3.13) between the X-axis disturbance F_x and the X-axis hand unit displacement x of the multi-axis system. All the influences from the Y-axis are treated as minor disturbance sources and should be suppressed by the parallel PI controller.

The D.O. design for the multi-axis system follows the same procedure mentioned in section 4.3.1. The designed D.O. is tested in both Simulink and on FPGA hardware, as shown in Figure 4-10. Despite the errors and phase lag induced by the number rounding, model simplification, and low-pass filter, the observer successfully captures the primary features and peaks of the disturbance.

With the same double PI controller in section 4.3.1 added parallel to the controller, the controller is first tested when both X-axis and Y-axis vibration actuators are connected to the hand unit with stingers. However, only the X-axis vibration actuator is applying a disturbance to the hand unit. The performance of the controller is presented in Figure 4-11. As shown in the figure, the maximum peak of hand unit displacement is reduced from 445 μm to 275 μm, and the maximum peak of FOUP acceleration is reduced from 4.70 m/s^2 to 4.09 m/s^2.

The Y-axis controller is designed using the same procedure as the X-axis controller, and the two controllers are combined together to suppress vibrations along both axes simultaneously. The performance of the multi-axis controller is evaluated by turning on the vibration generation and suppression along both axes simultaneously.

The controller performance shown in Figure 4-12 indicates that the designed multi-axis DOBC can suppress the hand unit and FOUP vibration in both travel (X-axis) and lateral (Y-axis) directions simultaneously. Along the X-axis, the maximum hand unit displacement peak is reduced from 816.25 μm to 506.25 μm, and the maximum

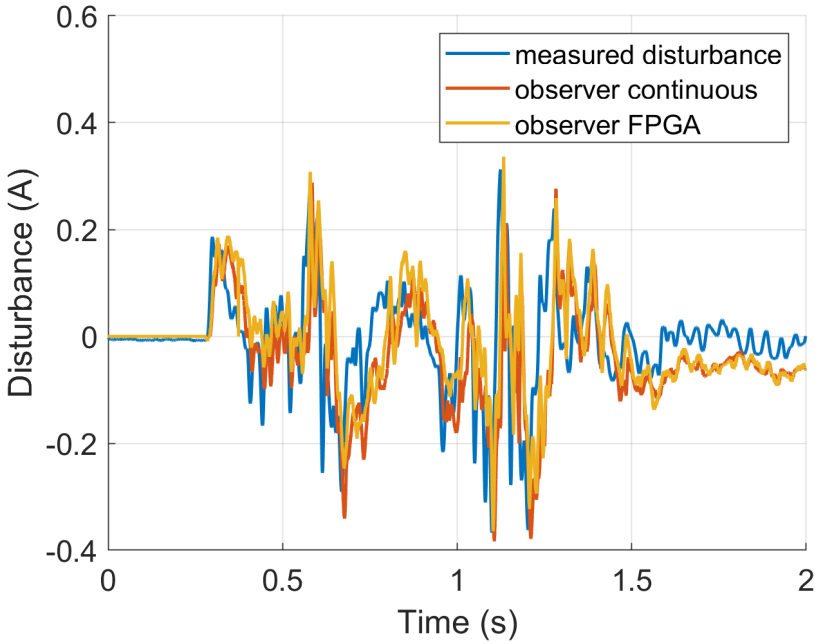

Figure 4-10: Multi-axis testbed-hand unit-FOUP system disturbance observer (D.O.) simulation in the X-axis. The blue curve represents the real input current of the disturbance actuator, which is proportional to the input disturbance; the red curve represents the observed disturbance from the measured displacement in Simulink; the yellow curve represents the observed disturbance with the discrete D.O. on hardware FPGA. [1]

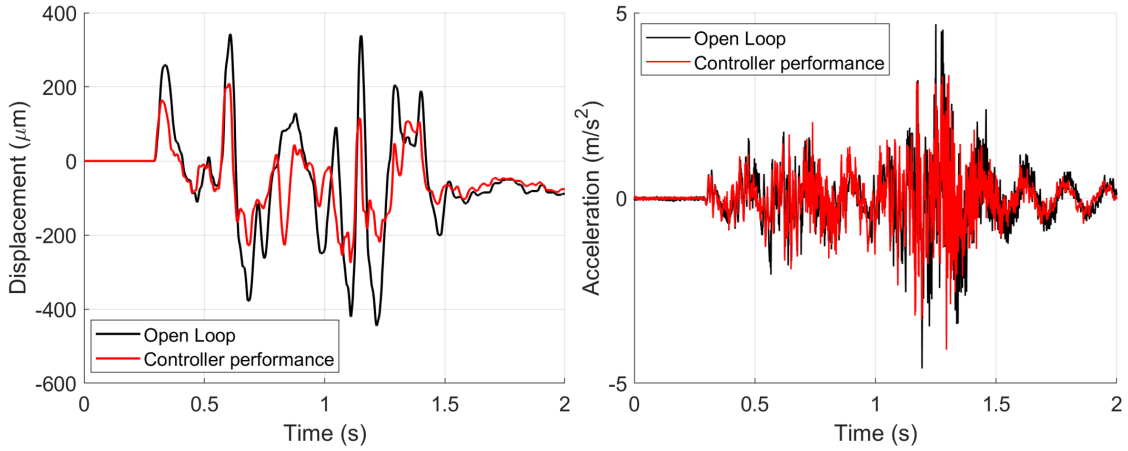

Figure 4-11: The performance of the X-axis Disturbance Observer-Based Controller (DOBC) on the multi-axis testbed-hand unit-FOUP system. Left: The black curve represents the hand unit displacement in the X-axis with a designed disturbance input in the open loop, and the red curve represents that in the controlled closed loop; Right: the black curve represents the FOUP acceleration in the X-axis in the open loop, and the red curve represents that in the controlled closed loop. [1]

FOUP acceleration peak is reduced from 6.11 m/s^2 to 3.53 m/s^2. In the Y-axis, the maximum hand unit displacement peak is reduced from 736.25 μm to 538.75 μm, and the maximum FOUP acceleration peak is reduced from 3.85 m/s^2 to 2.59 m/s^2.

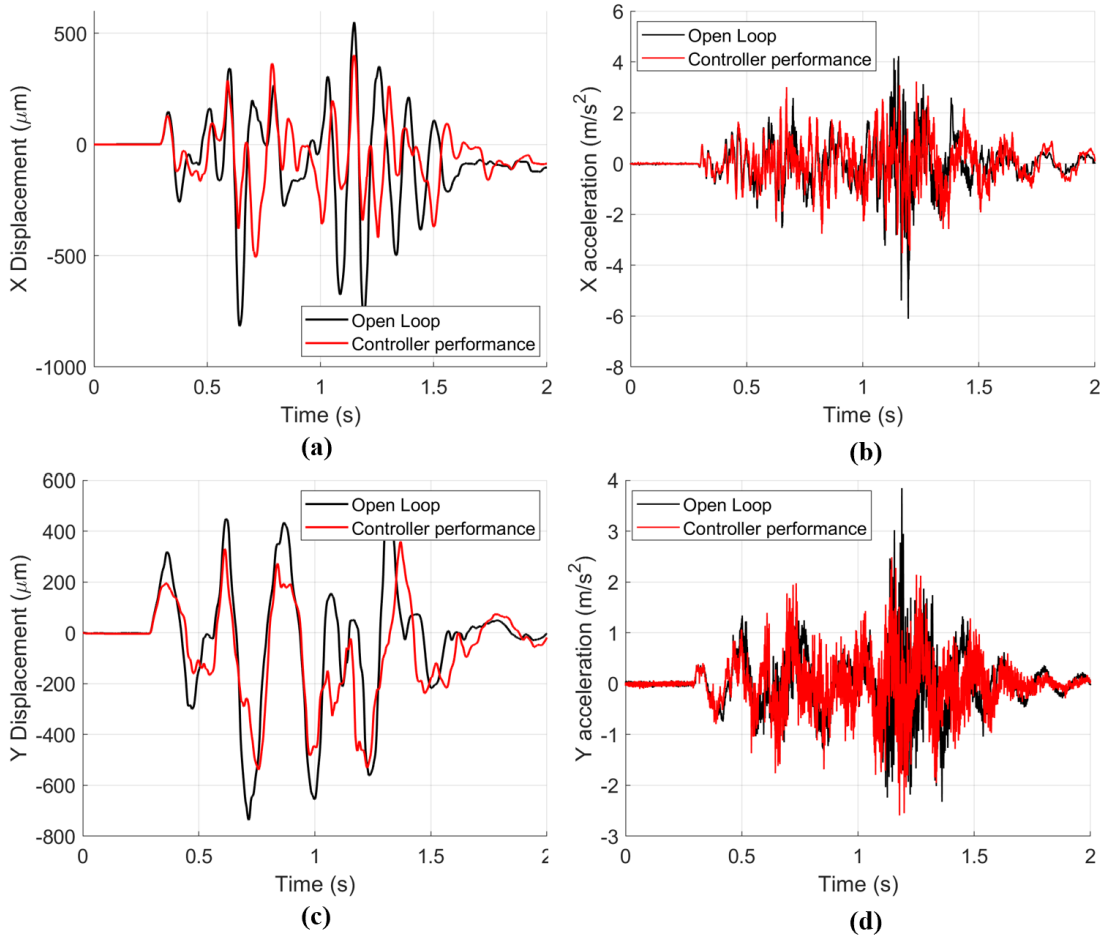

Figure 4-12: The performance of the multi-axis Disturbance Observer-Based Controller (DOBC) on the multi-axis testbed-hand unit-FOUP system. All the black curves are open-loop measurements, and all the red curves are controlled closed-loop measurements. (**a**): the hand unit displacement in X-axis; (**b**): the FOUP acceleration in X-axis; (**c**): the hand unit displacement in X-axis; (**d**): the FOUP acceleration in X-axis. [1]

4.4 Summary

This chapter focuses on the control algorithm design to suppress the vibration displacement of the hand unit and the vibration acceleration of the FOUP. First, PID

controller is selected as a benchmark, and the Disturbance Observer-Based Controller (DOBC) is selected as the appropriate type of control technique for this task. Next, a systematic approach is employed by starting from a simpler system and gradually increasing the complexity. The approach begins with the testbed-hand unit system in the travel direction (X-axis). Both the PID controller and the DOBC are tested and compared, and the DOBC is selected for better performance in the rest of the chapter. After that, the FOUP is added to the system, and a DOBC is developed for the single-axis testbed-hand unit-FOUP system. The performance shows that suppressing the hand unit displacement helps to reduce the FOUP acceleration, and the DOBC can observe the main disturbance in the designed direction. Finally, the multi-axis DOBC is designed for the X and Y axes of the multi-axis testbed-hand unit-FOUP system and tested. It shows that the designed DOBC can suppress the hand unit and FOUP vibration in both travel (X-axis) and lateral (Y-axis) directions simultaneously, indicating the effectiveness of the approach for practical application in semiconductor fabrication plants.

Chapter 5

Conclusions and Future Work

5.1 Conclusions

This thesis presents the development of a customized active vibration suppression system that employs an inertia force-based counterbalancing technique for controlling the vibration of FOUP on a custom-built vibration testbed. The vibration that propagates to the FOUPs through the OHT hand unit in semiconductor fabrication plants originates from the OHT vehicle's travel motion on tracks. The study starts with the design of a vibration generation testbed that eliminates the need for an entire track and can accurately reproduce OHT vibration in the laboratory environment. This testbed applies disturbances to the OHT hand unit simultaneously in the traveling (X-axis) and lateral (Y-axis) directions. Using the fabricated vibration generation testbed, a vibration suppression system that employs the inertia force-based counterbalancing technique is applied to suppress the vibration of the hand unit and FOUP in both axes simultaneously.

Since no sensors are allowed on the FOUP, the current work focuses on the control of the OHT hand unit vibration to reduce the vibration transmitted to the FOUP, and verifies that the OHT vibration control effectively suppresses the FOUP vibration in multiple axes. To achieve this goal, the system modeling and identification are performed using the designed testbed to derive the numerical linear model for the inputs (F_x and F_y) and outputs (x and y).

A baseline PID controller and a Disturbance Observer-Based Controller (DOBC) are first designed based on a simplified system, and the performance are compared. The DOBC yields a 74% reduction in maximum peak displacement (870 μm to 230 μm) compared to a 64% reduction with the baseline PID controller (870 μm to 315 μm). Therefore, the DOBC is selected as the optimal controller. After that, the reduction in vibration peaks of the FOUP acceleration is also verified with an on-board sensor. The measurement proves that reducing the hand unit displacement leads to a reduction in the acceleration of the FOUP vibration. Finally, based on the identified multi-axis linear model, a DOBC is developed and implemented on the hardware in both axes. With the DOBCs turned on simultaneously in both X and Y axes, and with disturbance applied to both axes, the hand unit displacement is suppressed 38% in X-axis and 27% in Y-axis, and the FOUP acceleration is suppressed 42% in X-axis and 33% in Y-axis. The disturbance observer played a major role in eliminating the main disturbance dynamics, and the parallel PI controller handled the coupled dynamics inherent to our testbed design. These results indicate that the custom active vibration suppression system can effectively reduce both the hand unit and FOUP vibration in both the travel and lateral directions simultaneously, demonstrating the practical applicability of this approach in semiconductor fabrication plants.

The successful suppression of FOUP vibration levels is of great importance for the semiconductor industry as it ensures the preservation of wafers during OHT transportation, resulting in a significant reduction in semiconductor chip defects. Moreover, the active vibration suppression techniques presented in this work can also be applied to a wide range of other applications where low vibration levels are required, further increasing the potential impact of this research.

5.2 Discussion

With the multi-axis DOBCs concept verified, the control performance can be further improved by utilizing a larger counter-balancing VCA with a longer traveling

range and higher maximum force. This enables more effective suppression of large acceleration peaks and avoids the impact of the VCA as it reaches its range limit.

The momentum analysis of VCA capacity and the control task requirement shows that the selected VCA is not strong enough to accomplish the task. The current control VCA (VCAR0033-0224-00A; SUPT Motion) has a maximum output force of $F_{max} = 33$ N and maximum stroke of $2x = 22.4$ mm. The zero position of the coil is positioned at the midpoint of the stroke for dual-direction usage, thus the maximum displacement of the moving mass in each direction is $x = 11.2$ mm. With a moving mass (the magnet) of 1 kg, the maximum momentum that can be generated by the control VCA before the moving mass collides with the base can be calculated using Equation (5.1) to be $P_{max} = 0.86$ Ns.

$$P_{max} = Ft = F\sqrt{2x/\alpha} = F\sqrt{2xm/F} = \sqrt{2xmF} = 0.86 \text{ Ns} \tag{5.1}$$

Now calculate the momentum required to suppress the vibration peaks. Take the multi-axis open loop FOUP X-axis acceleration into consideration. The maximum acceleration occurs around 1.2 sec. By integrating the acceleration at that peak, it is found that the velocity change is 0.077 m/s^2. The total mass of the moving part (hand unit and FOUP) is 12 kg. Therefore, the momentum required to suppress that acceleration peak is 0.924 Ns, which exceeds the maximum momentum that the current actuator could offer. Furthermore, if the force demand calculated from the controller is less than the maximum output force of the actuator (F_{max}), the momentum gained from the vibration suppression system will be even smaller. As a result, the collision between the moving mass and the base would occur if the gains of the second PI controller are small.

After upgrading the vibrations suppression system with a more powerful actuator, the same control system design methodology can be used with some parameter tuning to improve the vibration suppression performance.

5.3 Future work

The future work includes

1. As mentioned in section 5.2, developing a more powerful inertia-based vibration suppression system and further optimization of the controller parameters would improve the performance.

2. To improve the vibration transfer characteristics of the clamping mechanism between the hand unit and FOUP and to minimize the vibration transferred, it is suggested to upgrade the spring-damper clamp system. As a part of ongoing work shown in appendix B, the design of flexures with embedded piezo actuators in the new clamp is being developed to potentially enable active control ability and further improve the vibration suppression performance.

3. The hand unit displacement measurement is done by a linear encoder mounted on the vibration generation VCAs. To implement the active vibration technique in semiconductor fabrication OHT systems, an onboard displacement sensor is needed. Replacing the linear encoder to a quadrant position photodiode detector is ongoing. The mounting design of the sensor is shown in appendix C.

4. The input disturbance force profile developed in section 3.3 does not perfectly replicate the vibration pattern of the OHT. One potential approach to improve the input disturbance force profile is displacement control. The idea is to create a displacement profile with a second derivative that matches the acceleration reference. If the hand unit follows the designed displacement profile, it will also move with the desired acceleration. As the transfer function Equation (3.8) between the input force and hand unit displacement has more poles than zeros, displacement control would be easier than the original acceleration control. The ongoing process of implementing displacement control is detailed in appendix D.

5. Although no sensors are allowed on the FOUP, the FOUP acceleration can still potentially be observed through techniques such as Kalman filters.

6. The specific mechanism of the friction causing phase lag in the system has yet to be determined and remains unknown at this time.

7. The "Zero-Order Hold" method used to discretize the disturbance observer in section 4.3 may not be the most appropriate approach. An alternative method that can be considered is the bi-linear transformation, which can provide more accurate results for the controller.

Appendix A

Abbreviations

The following abbreviations are used in this manuscript:

OHT	Overhead Hoist Transport
FOUP	Front Opening Unified Pod
TMD	Tuned Mass Damper
DOBC	Disturbance Observer-Based Controller
PID	Proportional Integral Derivative
AMHS	Automated Material Handling System
TPA	Transfer Path Analysis
CAD	Computer-Aided Design
VCA	Voice Coil Actuator
DAQ	Data Acquisition
NI	National Instrument
FPGA	Field Programmable Gate Array
D.O.	Disturbance Observer

Appendix B

Clamp design

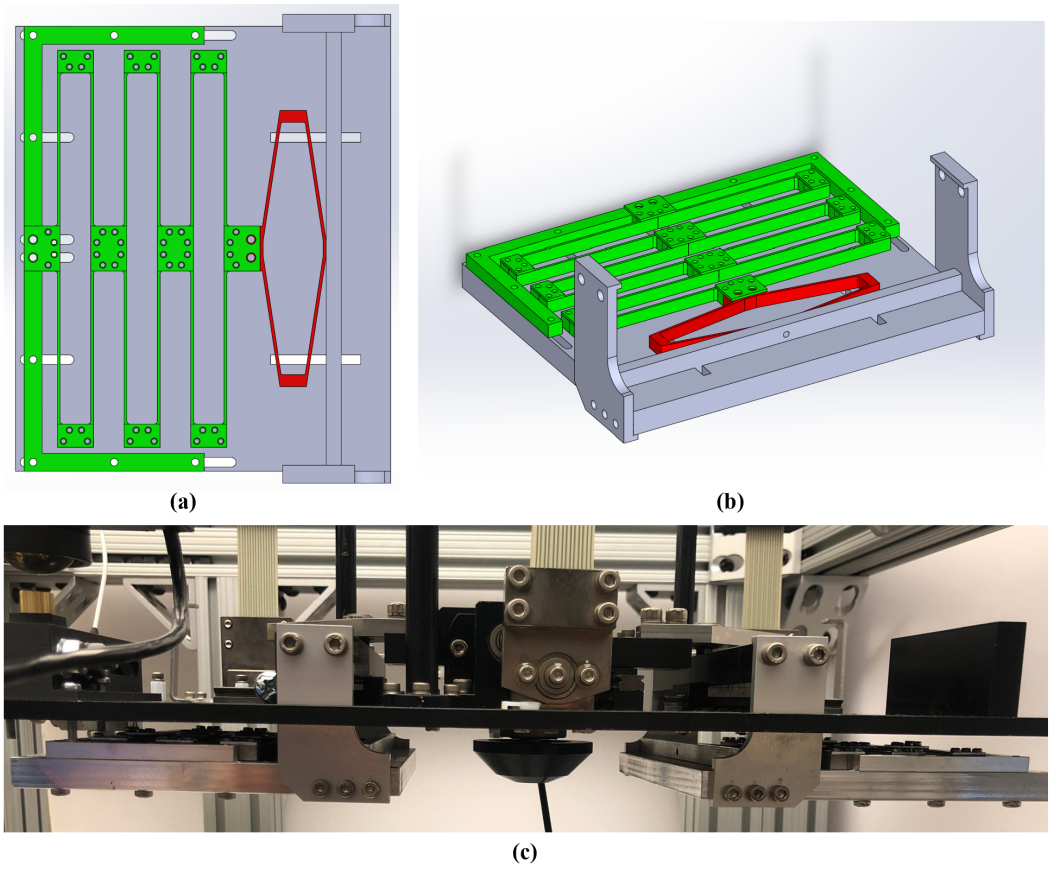

Figure B-1: New clamp design with adjustable stiffness and piezo actuator. (**a**) (**b**): The CAD of the new clamp design. The flexure part is highlighted in green. By fixing different flexure units together, the total stiffness can be adjusted. The piezo amplifier is highlighted in red (the piezo is not included in the CAD). This design allows active control. (**c**): the new clamp assembled onto the hand unit.

Appendix C

Quadrant position photodiode detector

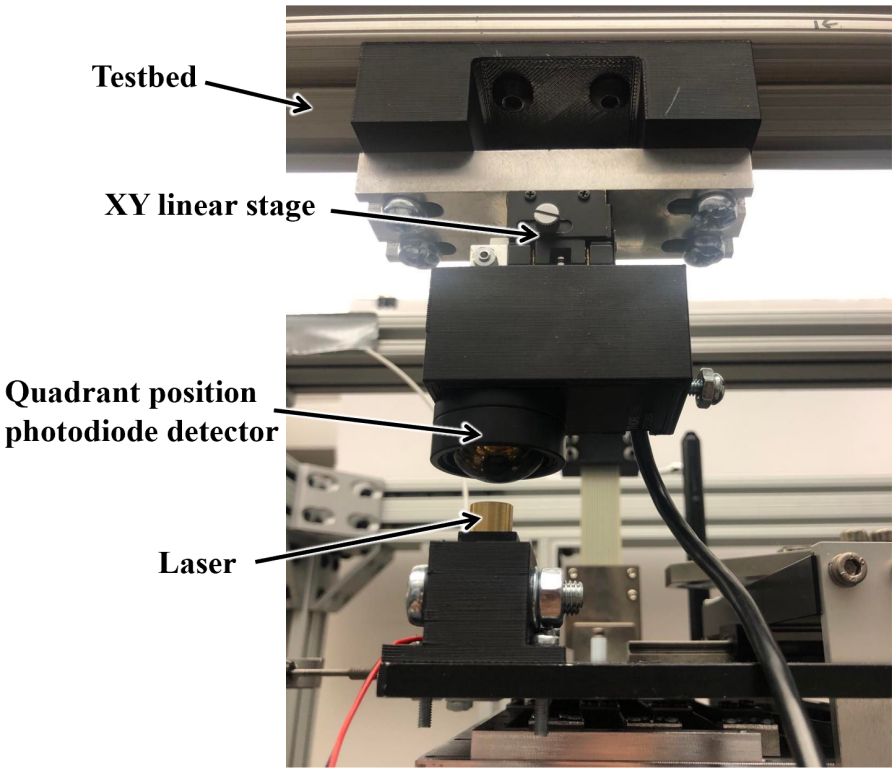

Figure C-1: Quadrant position photodiode detector mounted on the testbed and hand unit. The sensor is PDQ80A from Thorlabs. The laser is 0220-968-00 from Edmund Optics. The designed mounting system enables both coarse and precise adjustment of the alignment.

Appendix D

Displacement control

The displacement profile to be tracked is first designed, taking into consideration the limitation that the vibration generation testbed vibrates the system in place, and thus the displacement of the hand unit on the testbed cannot be too large. However, the collected acceleration data is from actual systems running on the tracks in Samsung plants, and the displacement of the raw acceleration data keeps increasing, which cannot be realized on the testbed. To address this, the DC component of the designed profile needs to be suppressed. This is done by passing the data through a high-pass filter with a passband frequency of 1 Hz in Matlab. The resulting designed displacement profile is shown in Figure D-1(a). The acceleration of designed displacement is compared with the reference acceleration in Figure D-1(b).

It is worth noting that there is a gradual acceleration period before the first peak in the acceleration profile at 0.3s, which corresponds to the OHT vehicle starting to speed up and move on the track. Therefore, when designing the displacement profile, the region of constant displacement increment is eliminated.

For the displacement controller design, the Matlab "Loop Shaping" tuning method is utilized with a target bandwidth of 200 Hz and the desired second-order controller. The optimized controller is shown in Equation (D.1).

$$C(s) = \frac{0.00725(s^2 + 81.36s + 4919)}{s(s + 1127)} \tag{D.1}$$

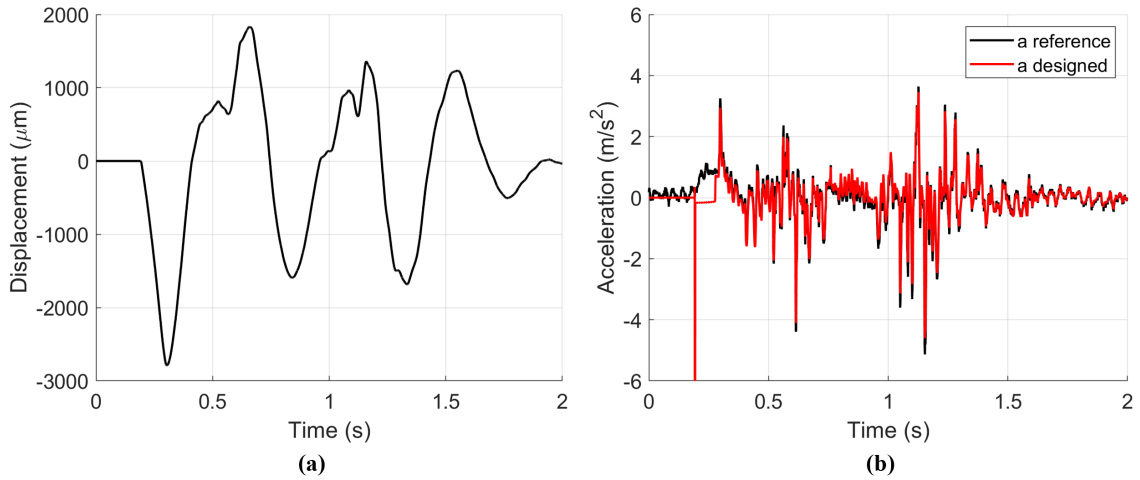

Figure D-1: (**a**) The profile of the displacement of the hand unit on the vibration generation testbed that is designed to match the acceleration reference collected from the hand unit in the Samsung plant. (**b**) A comparison between the acceleration reference (in black) and the acceleration resulting from the designed displacement profile (in red).

The iterative learning method is also applied here. The controller is composed of a feedforward part and a feedback part. For each iteration, the feedforward part is updated by the control effort in the last iteration. The controller structure is shown in Figure D-2.

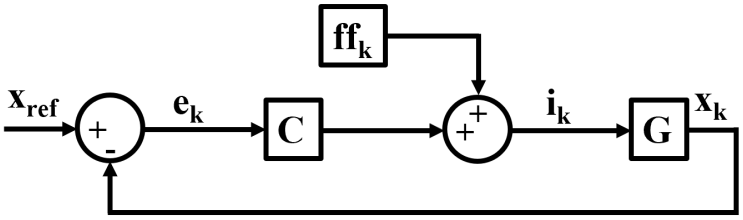

Figure D-2: Block diagram of the iterative learning displacement controller.

Here x_{ref} is the hand unit displacement reference; $e_k = x_{\text{ref}} - x_k$ is the control error of kth iteration; C is the controller shown in Equation (D.1); ff_k is the feedforward input current of kth iteration; i_k is the control effort of kth iteration; G is the plant, and x_k is the hand unit displacement of kth iteration.

The iteration law is shown in Equation (D.2). With the block diagram relationship Equation (D.3), the relationship between kth control error e_k and k+1th control error

e_{k+1} is thus shown in Equation (D.4).

$$\mathrm{ff}_{k+1} = i_k = \mathrm{ff}_k + Ce_k \tag{D.2}$$

$$x_k = \frac{G}{1+CG}\mathrm{ff}_k + \frac{CG}{1+CG}x_{\mathrm{ref}} \tag{D.3}$$

$$\begin{aligned} e_{k+1} &= x_{\mathrm{ref}} - x_{k+1} \\ &= x_{\mathrm{ref}} - \frac{G}{1+CG}\mathrm{ff}_{k+1} - \frac{CG}{1+CG}x_{\mathrm{ref}} \\ &= \frac{1}{1+CG}x_{\mathrm{ref}} - \frac{G}{1+CG}(\mathrm{ff}_k + Ce_k) \\ &= \frac{1}{1+CG}x_{\mathrm{ref}} - \left(x_k - \frac{CG}{1+CG}x_{\mathrm{ref}}\right) - \frac{CG}{1+CG}e_k \\ &= x_{\mathrm{ref}} - x_k - \frac{CG}{1+CG}e_k \\ &= \frac{1}{1+CG}e_k \end{aligned} \tag{D.4}$$

Equation (D.4) shows that as long as the magnitude of $|\frac{1}{1+CG}|$ is smaller than 1 (which means $|1+CG| > 1$), the displacement error will decrease through iteration. The Nyquist test is thus plotted together with a unit circle at [-1, 0] in Figure D-3. It shows that as frequency increases, CG in the complex domain will enter the unit circle, which means $|1+CG| < 1$ at high frequency. The critical frequency is 216 rad/s.

The controller is tested in Simulink first. The controlled displacement error e_k of the first three iterations are plotted in Figure D-4. As shown in Figure D-4(a), with more iterations conducted, the amplitude of the error is decreased. As shown in Figure D-4(b), the low-frequency error decreases while the high-frequency error increases with more iterations, which meets with the Nyquist test result.

The controller is also tested on the hardware. The controlled displacement error e_k of the first three iterations are plotted in Figure D-5. Similar to the simulated result, both the time domain performance and the frequency domain performance

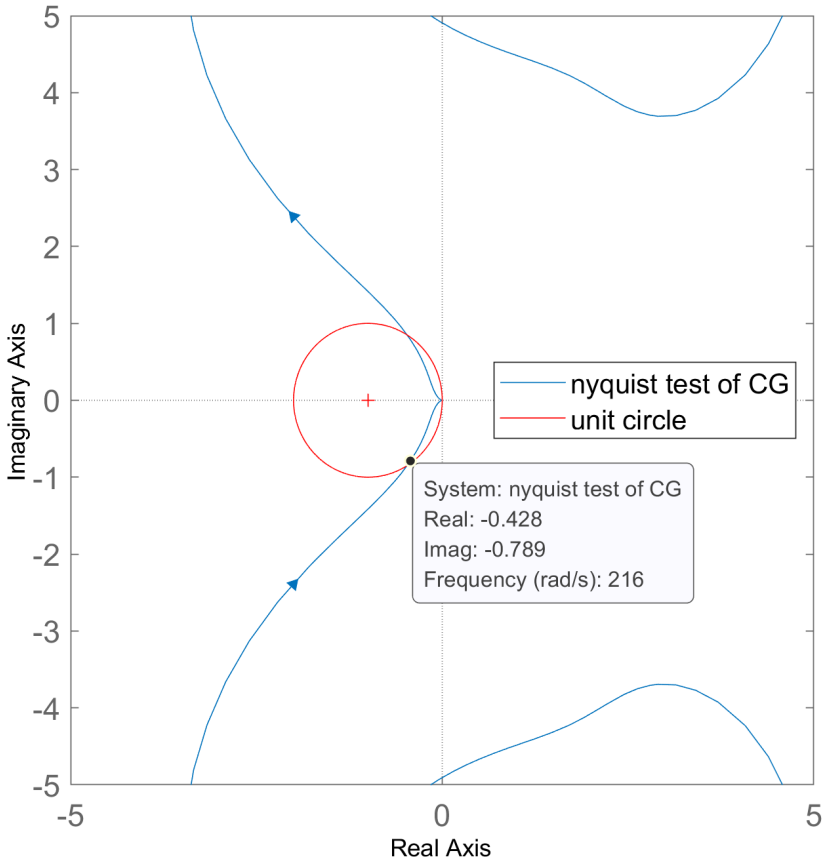

Figure D-3: Nyquist test of the hand unit displacement controller.

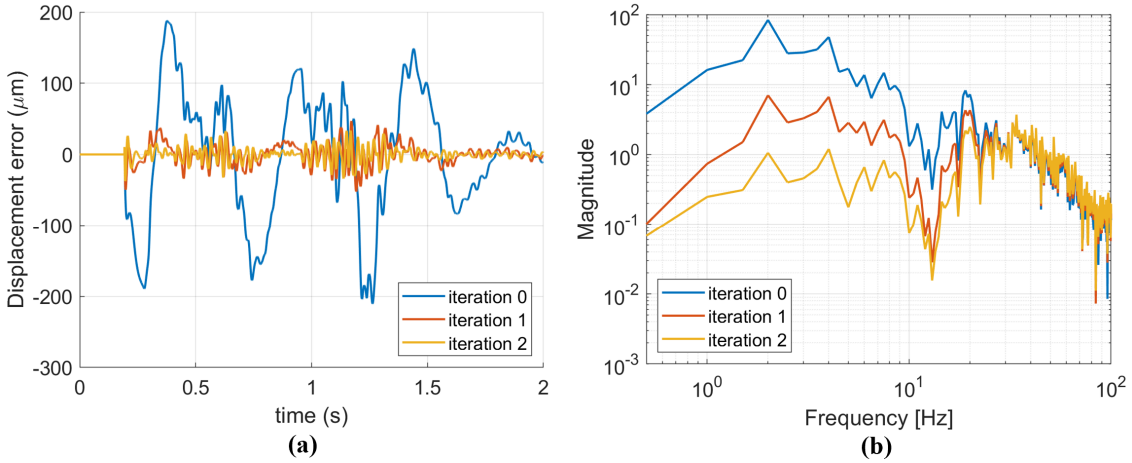

Figure D-4: The simulated controlled hand unit displacement error. The first, second, and third iteration results are plotted in blue, red, and yellow. (**a**): time domain plot. (**b**): frequency domain plot.

meet with the Nyquist test result. However, in Figure D-5(a), the error in the time domain decreases slower than in the simulation. In Figure D-5(b), the error in the frequency domain starts to increase after 12 Hz, while in the Nyquist test the critical frequency is 216 rad/s (34.38 Hz). This extra error is caused by the quantization of the digital linear encoder.

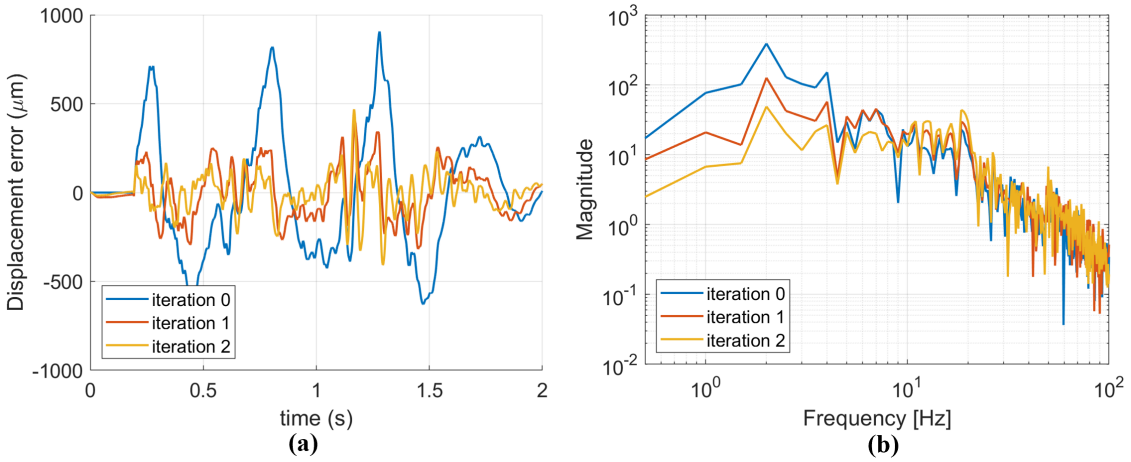

Figure D-5: The tested controlled hand unit displacement error. The first, second, and third iteration results are plotted in blue, red, and yellow. (**a**): time domain plot. (**b**): frequency domain plot.

Due to the error caused by the quantization, the acceleration has a large high-frequency error after iteration. This method is still in process. The analog onboard quadrant position photodiode detector may improve the performance.

Bibliography

[1] Jiajie Qiu, Hongjin Kim, Fangzhou Xia, and Kamal Youcef-Toumi. Multi-axis active vibration suppression for wafer transfer systems. In *2023 IEEE/ASME International Conference on Advanced Intelligent Mechatronics (AIM)*, 2023.

[2] Jiajie Qiu, Hongjin Kim, Fangzhou Xia, and Kamal Youcef-Toumi. Disturbance rejection control for active vibration suppression of overhead hoist transport vehicles in semiconductor fabs. *Machines*, 11(2):125, 2023.

[3] C-H Kuo. Modelling and performance evaluation of an overhead hoist transport system in a 300 mm fabrication plant. *The International Journal of Advanced Manufacturing Technology*, 20(2):153–161, 2002.

[4] Da-Yin Liao, Shi-Chung Chang, Kuo-Wei Pei, and Chi-Ming Chang. Daily scheduling for r&d semiconductor fabrication. *IEEE transactions on semiconductor manufacturing*, 9(4):550–561, 1996.

[5] Sara Case, Stephanie Waite, John Barker, Wei Zhao, Jong Soo Kim, Joshua Moore, and Eswar Ramanathan. Impact of foup environment on product yield in advanced technologies. In *2016 27th Annual SEMI Advanced Semiconductor Manufacturing Conference (ASMC)*, pages 168–171. IEEE, 2016.

[6] D. Dance and K. Gildersleeve. Estimating semiconductor yield from equipment particle measurements. In *[1992 Proceedings] IEEE/SEMI International Semiconductor Manufacturing Science Symposium*, pages 18–23, 1992.

[7] Yoshiaki Kobayashi, Shigeru Kobayashi, Kenji Tokunaga, Koji Kato, and Teruo Minami. Particle characteristics of 300-mm minienvironment (foup and lpu). *IEEE transactions on semiconductor manufacturing*, 13(3):259–263, 2000.

[8] Aly Mousaad Aly. Vibration control of high-rise buildings for wind: a robust passive and active tuned mass damper. *Smart Structures and Systems*, 13(3):473–500, 2014.

[9] Said Elias and Vasant Matsagar. Research developments in vibration control of structures using passive tuned mass dampers. *Annual Reviews in Control*, 44:129–156, 2017.

[10] Haoran Zuo, Kaiming Bi, and Hong Hao. Using multiple tuned mass dampers to control offshore wind turbine vibrations under multiple hazards. *Engineering Structures*, 141:303–315, 2017.

[11] CR Fuller and AH Von Flotow. Active control of sound and vibration. *IEEE Control Systems Magazine*, 15(6):9–19, 1995.

[12] Fu-Cheng Wang, Chung-Hung Yu, Jeff Tsung-Hui Tsai, and San-Ho Yang. Decoupled robust vibration control of an optical table. *Journal of Vibration and Control*, 20(1):38–50, 2014.

[13] Peter Heiland. Active vibration isolation system, March 25 2014. US Patent 8,682,609.

[14] Nan-Chyuan Tsai, Din-Chang Chen, Li-Wen Shih, and Chao-Wen Chiang. Model reduction and composite control for overhead hoist transport system by singular perturbation technique. *Journal of Vibration and Control*, 18(8):1081–1095, 2012.

[15] Hirotaka Tokoro, Motohiro Kawafuku, and Makoto Iwasaki. An application of state feedback control to actual vehicle vibration suppression. In *2014 IEEE 13th International Workshop on Advanced Motion Control (AMC)*, pages 185–190. IEEE, 2014.

[16] Shuyou Yu, Jing Wang, Yan Wang, and Hong Chen. Disturbance observer based control for four wheel steering vehicles with model reference. *IEEE/CAA Journal of Automatica Sinica*, 5(6):1121–1127, 2016.

[17] Juha Plunt. Finding and fixing vehicle nvh problems with transfer path analysis. *Sound and vibration*, 39(11):12–17, 2005.

[18] Maarten V van der Seijs, Dennis de Klerk, and Daniel J Rixen. General framework for transfer path analysis: History, theory and classification of techniques. *Mechanical Systems and Signal Processing*, 68:217–244, 2016.